



JGR Solid Earth

RESEARCH ARTICLE

10.1029/2022JB024518

Key Points:

- We present a new model for anisotropic rock damage under the influences of biotite weathering, regional stresses, and topographic
- Simulations show that under common topographic and tectonic conditions, microcrack propagation can be far more sensitive to biotite weathering than far-field stresses
- Biotite weathering produces shear stress zones at the bottom of hillslopes, vertical tension below hilltops and horizontal compression in valleys

Correspondence to:

C. Arson, chloe.arson@ce.gatech.edu

Citation:

Xu, T., Shen, X., Reed, M., West, N., Ferrier, K. L., & Arson, C. (2022). Anisotropy and microcrack propagation induced by weathering, regional stresses and topographic stresses. *Journal of Geophysical Research: Solid Earth*, 127, e2022JB024518. https://doi.org/10.1029/2022JB024518

Received 5 APR 2022 Accepted 5 JUL 2022

Anisotropy and Microcrack Propagation Induced by Weathering, Regional Stresses and Topographic Stresses

Tingting Xu¹, Xianda Shen², Miles Reed³, Nicole West⁴, Ken L. Ferrier³, and Chloé Arson¹

¹Georgia Institute of Technology, Atlanta, GA, USA, ²Clarkson University, Potsdam, NY, USA, ³University of Wisconsin-Madison, Madison, WI, USA, ⁴Central Michigan University, Mount Pleasant, MI, USA

Abstract This paper presents a new model for anisotropic damage in bedrock under the combined influences of biotite weathering, regional stresses, and topographic stresses. We used the homogenization theory to calculate the mechanical properties of a rock representative elementary volume made of a homogeneous matrix, biotite inclusions that expand as they weather, and ellipsoidal cracks of various orientations. With this model, we conducted a series of finite element simulations in bedrock under gently rolling topography with two contrasting spatial patterns in biotite weathering rate and a range of biotite orientations. In all simulations, damage is far more sensitive to biotite weathering than to topographic or regional stresses. The spatial gradient of damage follows that of the imposed biotite weathering rate at all times. The direction of micro-cracks tends to align with that of the biotite minerals. Relative to the topographic and regional stresses imparted by the boundary conditions of the model, the stress field after 1,000 years of biotite weathering exhibits higher magnitudes, wider shear stress zones at the feet of hills, more tensile vertical stress below the hilltops, and more compressive horizontal stress concentrated in the valleys. These behaviors are similar in simulations of slowing eroding topography and static topography. Over longer periods of time (500 kyr), the combined effects or weathering and erosion result in horizontal tensile stress under the hills and vertical tensile stress under and in the hills. These simulations illustrate how this model can help elucidate the influence of mineral weathering on Critical Zone evolution.

Plain Language Summary In bedrock, stresses are generated through a combination of chemical weathering, topography, and tectonic forces. Together, these disaggregate minerals and redistribute stress, thereby damaging the rock. In this study, we focus on the sensitivity of rock damage to the weathering of biotite, which expands as it weathers and pushes on the surrounding minerals. We propose a micro-mechanical model in which small cracks grow in response to biotite weathering. The mechanical properties of the bulk rock are obtained by homogenization. With this model, we conducted a series of finite element simulations in bedrock under gently rolling topography, two contrasting spatial patterns in biotite weathering rate, and a range of biotite orientations. In our simulations, the spatial distribution of rock damage always follows that of biotite weathering. This shows that crack growth is far more sensitive to biotite weathering than to the topographic or regional stresses applied in these simulations. These simulations also highlight the importance of the direction of the biotite minerals relative to the regional stress field. Together, these simulations show that biotite weathering is capable of dominating the development of bedrock damage. More generally, these simulations show that the proposed model can be used as a tool to explore the influence of mineral weathering on Critical Zone evolution.

1. Introduction

The zone of weathered and fractured regolith between fresh bedrock and mobile soil is of wide interest. It is a common feature of terrestrial landscapes (Graham et al., 1994; Riebe et al., 2021) and it forms the thickest portion of the Critical Zone—the region between the top of the forest canopy and unweathered bedrock at depth—in many regions (Buss et al., 2008; Callahan et al., 2020; Flinchum et al., 2018; Holbrook et al., 2019; Pavich et al., 1989). The thickness and material properties of this weathered layer influence the pace of landscape evolution (Dixon et al., 2009), the capacity of landscapes to retain water through drought (Salve et al., 2012), and the degree and type of landsliding a given area is subject to (Watakabe & Matsushi, 2019). Because much of a landscape's chemical erosion can occur in this immobile regolith (Dixon et al., 2012), the minerals supplied to this layer are an important source of nutrients and a key regulator of climate through silicate weathering (Ferrier

© 2022. American Geophysical Union. All Rights Reserved.

XU ET AL. 1 of 37



et al., 2016; Walker et al., 1981). Thus, the formation of this weathered layer is a vital component of feedbacks between topography, climate, and ecology.

For the sake of brevity in this study, we refer to this layer as saprolite, while recognizing that it is variously referred to as weathered rock or the physically immobile portion of the Critical Zone. For our purposes, the important characteristics of this layer are that it is subject to mechanical damage and chemical alteration relative to the underlying bedrock, and that it is physically static—that is, it is not transported downslope by physical erosion.

The controls on the formation and evolution of saprolite are incompletely understood, in part because it is challenging to measure rates of saprolite production and evolution over the long residence times and large depths of many saprolites. A critical component in the evolution of saprolite is the initiation of damage. In this study, we use the term damage to refer to the variable that quantifies the amount of energy dissipation that is induced by crack propagation and that leads to a decrease of stiffness and strength. Fracture inception and propagation by weathering processes such as biotite expansion, frost cracking, and tree root wedging can be thought of as rock damage as there is attendant degradation of rock strength (Anderson et al., 2013; Fletcher et al., 2006; Roering et al., 2010). Within the Critical Zone, the transition from intact rock to saprolite is often accompanied by changes in characteristics correlated with rock damage, such as fracture density, porosity, or seismic wave speed (Buss et al., 2008; Callahan et al., 2020; Goodfellow et al., 2016; Hayes et al., 2019; Holbrook et al., 2019).

One long-hypothesized driver of bedrock weakening is biotite weathering. Biotite expands during iron oxidation, generating stresses that can initiate microfractures, reduce rock strength, create connected porosity, and promote chemical weathering of other mineral phases (Buss et al., 2008; Fletcher et al., 2006; Goodfellow et al., 2016; Isherwood & Street, 1976; Nettleton et al., 1970; Wahrhaftig, 1965). Fletcher et al. (2006) modeled the buildup of stress energy by biotite expansion in a corestone and highlighted that this expansion can lead to the formation of corestone-bounding fractures. Goodfellow et al. (2016) showed evidence for distributed microcracking of the surrounding rock matrix upon oxidation and a coincident reduction in rock strength. The mechanism has been shown to operate in diverse environments, from slowly eroding, tropical uplands (Behrens et al., 2015; Hewawasam et al., 2013) to more rapidly eroding Mediterranean scrub (Jiang & Lee, 2019; Vierra et al., 2018). These studies suggest that biotite characteristics (e.g., abundance and orientation) may influence landscape-scale patterns of damage and stress in immobile regolith. For example, since biotite only expands along the basal cleavage plane (Dong et al., 1998), rock with a dominant biotite orientation could lead to immobile regolith with anisotropic damage and stress fields (Leone et al., 2020).

The production of rock damage by biotite weathering is distinct from other processes that also damage rock. For instance, rock damage can be generated by regional stress fields caused by far-field tectonic processes (Slim et al., 2015). Similarly, a combination of topographically-generated and regional stresses can lead to a preferential opening of fractures of certain orientations, which can compete with or enhance other fracture generating processes (Moon et al., 2017, 2020). So far, models incorporating topographic stress have not been directly coupled to a model with a physico-chemical mechanism of rock damage. Mechanisms for environmentally dependent subcritical crack growth include stress corrosion, dissolution, ion exchange and microplasticity. Formulations based on the concept of stress corrosion have been proposed to predict time-dependent cracking and brittle creep behavior, which allowed understanding delayed failure in a variety of lithologies (Brantut et al., 2012, 2013; Stefanou & Sulem, 2014) and simulation of borehole spalling and breakout (Schoenball et al., 2014). Detailed image recordings of progressive rock slope failure have also highlighted the role of stress redistribution during the propagation of sheeting joints (Stock et al., 2012). Several studies posit that the evolution of the Critical Zone is driven by subcritical fracture propagation. For example, Walder and Hallet (1985) developed a detailed theoretical model of rock fracture due to freezing, delineating precisely the effects of environmental conditions on frost cracking. Eppes and Keanini (2017) found that most mechanical weathering at and near Earth's surface is likely driven by superimposed sources of low-magnitude subcritical stresses. These advances in modeling crack propagation are directly applicable to—but have seldom been applied to—the evolution of stress and damage in the Critical Zone.

Here, we develop a model to explore the influence of biotite expansion on the development of anisotropic damage and stress in rock. To this end, we extend the damage model in Shen et al. (2019) to include microcracks capable of opening, closing and propagating. Our approach involves considering a Representative Elementary Volume (REV) of rock, which we model as a composite made of biotites and cracks embedded in a homogeneous matrix.

XU ET AL. 2 of 37



This three-phase system is intended to focus on the effects of biotite weathering on the surrounding minerals of the bedrock, which are represented as a homogeneous matrix. The only damage mechanism considered here is mechanical microcrack propagation as a result of the redistribution of stress induced by the expansion of biotite minerals during weathering. In that context, the macroscopic scale represents the REV scale, while the microscale refers to the scale of the cracks or biotite inclusions.

To compute the evolution of REV characteristics over time, we use Eshelby's homogenization theory (Eshelby, 1957), in which biotites and cracks are viewed as inclusions gathered in sets. An inclusion set is characterized by micro-structure properties (such as size, shape, orientation) and/or material properties (such as mechanical behavior or chemical potential). By contrast with phenomenological models, in which the damage variable is updated through an evolution law defined at REV scale in the same way as in the theory of plasticity, homogenization-based models such as the one proposed here are formulated with crack densities calculated at micro-scale by means of fracture mechanics principles such as Griffith energy based propagation criterion. The micro-crack densities are then used to calculate a damage variable that describes the state of the REV. Homogenization-based models are powerful because they provide both an explanatory and a predictive framework to complex macroscopic behaviors (Arson, 2020).

The paper is organized as follows. Section 2 explains the homogenization approach used in this study. Section 3 describes the equilibrium equations that govern the mechanical behavior of the rock constituents that make up the REV, mainly, the rock matrix, the biotite inclusions, and the cracks. Section 4 presents a set of simulations at REV scale that highlight the effects of biotite weathering on damage and damaged stiffness, as well as their sensitivity to depth, biotite orientation, and damage evolution parameters. Section 5 reports the results of finite element (FE) simulations in rock under sinusoidal topography, which we use to study the effects of biotite orientation and spatial patterns in biotite weathering rate on stresses and damage over 1,000 years of weathering. Section 6 extends the FE simulations to topographies that undergo surface erosion. These simulations show that biotite expansion can cause local stress field rearrangement and microcracking in the presence of far-field and topographic stress fields. These simulations also show that the magnitudes and patterns of anisotropic rock damage depend on biotite orientation, with implications for future near-surface geophysical surveys (Eppinger et al., 2021; Novitsky et al., 2018). In all simulations, the spatial distribution of rock damage follows that of the imposed biotite weathering gradient, thus highlighting the potential for biotite expansion to damage rock and perturb subsurface stress fields. Implications for the evolution of the Critical Zone are discussed in Section 7. Lastly, we draw the main conclusions of this study in Section 8.

We note vectors with lower case letters underlined by a single bar, for example, \underline{n} is the normal vector. Second order tensors are noted with boldface letters: for example, ϵ , σ are respectively the strain and the stress tensor, and I is the second-order identity tensor. Fourth order tensors are noted with blackboard bold letters: for example, \mathbb{M} represents the compliance tensor. Cartesian coordinates are used and the convention of summation on repeated indices is adopted. Tensor algebraic operations used in this paper are the following:

$$\boldsymbol{\sigma} \cdot \underline{\boldsymbol{n}} = \sigma_{ij} \boldsymbol{n}_j \tag{1}$$

$$\mathbb{M}: \boldsymbol{\sigma} = M_{ijkl}\sigma_{kl}, \ \mathbb{P}: \ \mathbb{C} = P_{ijkl}C_{klmn}$$
 (2)

$$\underline{m} \otimes \underline{n} = m_i n_j \tag{3}$$

$$\left(a\overline{\underline{\otimes}}b\right)_{ijkl} = \frac{1}{2}\left(a_{ik}b_{jl} + a_{il}b_{jk}\right) \tag{4}$$

I is the fourth-order identity tensor of components in an orthonormal frame:

$$I_{ijkl} = \frac{1}{2} \left(\delta_{ik} \delta_{jl} + \delta_{il} \delta_{jk} \right) \tag{5}$$

in which δ_{ij} is the Kronecker delta function. The hydrostatic projection tensor \mathbb{J} and the deviatoric projection tensor \mathbb{K} are respectively defined as:

XU ET AL. 3 of 37



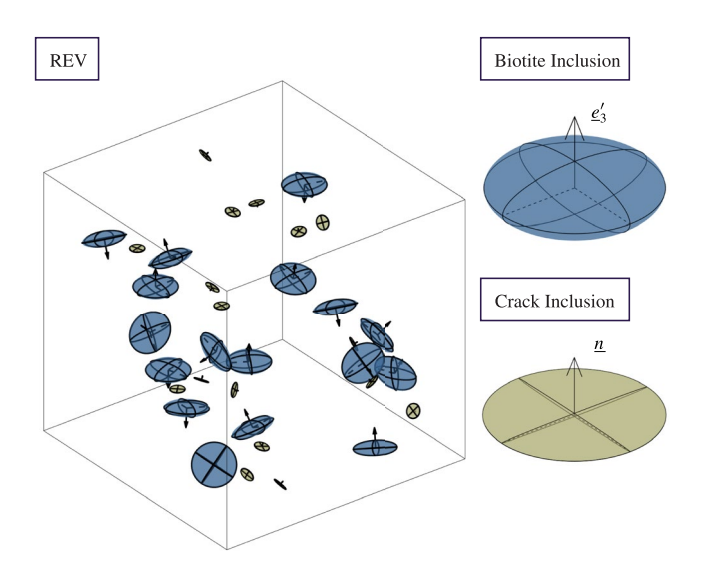


Figure 1. Sketch of a three-dimensional Representative Elementary Volume of rock considered in the proposed model. The superscript m refers to the matrix. Ellipsoidal biotite inclusions are characterized by their expansion direction, represented by e_3' in the local coordinate system attached to the biotite inclusions. Microcracks are characterized by their orientation, represented by the vectors normal to their planes (\underline{n}) . Here, it is assumed that the micro-cracks are one to two orders of magnitude smaller than the biotite minerals.

$$J_{ijkl} = \frac{1}{3}\delta_{ij}\delta_{kl} \tag{6}$$

$$\mathbb{K} = \mathbb{I} - \mathbb{J} \tag{7}$$

J and K obey the following algebraic properties:

$$J: J = J, K: K = K, J: K = K: J = 0$$
(8)

The partial derivative of a function f with respect to the variable x is denoted by $\frac{\partial f}{\partial x}$ or $\partial_x f$.

2. Upscaling Technique: Two-Step Mori-Tanaka Homogenization Scheme

Our overarching goal in this study is to develop a model to compute the temporal and spatial evolution of rock stress, strain and damage. For this, we turn to a homogenization approach.

At its core, our model is based on the behavior of a rock REV, the size of which is statistically defined as a domain of size λ^3 , in which λ is the minimum distance over which the variance of mechanical properties (such as the stiffness tensor) is zero. The key to the description of micro-crack propagation as the result of weathering is an appropriate representation of the microstructure of rock, which influences the calculation of the damage conjugate force, hence the crack propagation criteria and the damaged stiffness of the REV.

Here, we are particularly interested in the effects of biotite weathering on the propagation of microcracks, which perturb the stress field. Biotite expands

significantly during the early stages of weathering as potassium cations are replaced by hydrated magnesium cations between sheet silicate layers, and thus is a good model mineral to study the influence of mineral weathering on bedrock stress redistribution. We thus consider that the REV is made of biotite inclusions and microcracks, each with different mechanical properties and orientations, embedded in a homogeneous matrix (see Figure 1). As explained in the introduction, the macroscopic scale represents the REV scale, while the microscale refers to the scale of the cracks or biotite inclusions. In the simulations we present later in this study, the REV size λ is \sim 0.1 m, such that the REV volume is \sim 0.001 m³. In this section, we explain how the stiffness of the REV is calculated based upon the knowledge of the stress and strain fields in the biotite inclusions, cracks and rock matrix. Section 3 describes the mechanical behavior of the REV constituents (biotite, cracks and matrix).

The model formulated here builds on the model we developed in Shen et al. (2019) and extends it by coupling the expansion of biotite inclusions (due to weathering) to the propagation of sets of micro-cracks in the rock matrix. In Shen et al. (2019), damage was a scalar quantity and the evolution of damage was following phenomenological (empirical) laws. The mathematical formulation presented here is more complex, because micro-cracks are represented explicitly, their evolution depends on micro-mechanical balance equations, and at the REV level, damage is anisotropic.

2.1. Calculating Homogenized REV Properties Using the Mori-Tanaka Scheme

Key to understanding the evolution of rock damage during mineral weathering is the calculation of the average stress and strain fields in a REV. For this purpose, we adopt a Mori-Tanaka homogenization scheme to calculate REV-scale field variables (e.g., the stress and strain tensors and the macroscopic crack density tensor) and mechanical properties (e.g., the REV damaged stiffness tensor) (Benveniste, 1987; Mori & Tanaka, 1973). The Mori-Tanaka scheme is based on Eshelby's theory (Eshelby, 1957), which proves that the stress and strain fields inside an ellipsoidal inclusion are uniform. In the homogenization theory, an inclusion is a part of the REV that

XU ET AL. 4 of 37



is subjected to a so-called "eigenstrain", which is a generic name for inelastic strains such as thermal expansion, phase transformation initial strain, plastic strain, and misfit strain (Mura, 1987).

Here, the REV is a multi-phase system made of biotite inclusions and cracks embedded in a homogeneous matrix (Figure 1). This simplification allows us to focus on the mechanical effect of the constrained expansion of biotite minerals embedded in the bedrock matrix. The biotite eigenstrain produced by chemical weathering is the driver of what we call "weathering-induced damage" in the matrix in the following. We adopt a mathematical representation that allows prediction of crack propagation in any direction of space, by means of a numerical integration scheme that accounts for 74 discrete orientations over the unit sphere (Bažant & Oh, 1986). Microcracks are heterogeneities that exhibit mechanical properties different from that of the matrix but that do not present any stress or strain independent from the far field stress or strain. Cracks are represented as equivalent inclusions in the sense of the homogenization theory, which means that the difference of mechanical stiffness between the matrix and the cracks is represented by an equivalent eigenstress or eigenstrain. Biotite minerals are heterogeneities that are endowed with a chemical strain field (induced by weathering) that is independent from the boundary conditions and is thus an eigenstrain field. Biotite minerals are thus heterogeneous inclusions in the sense of the theory of homogenization, and can also be modeled as equivalent inclusions. All of the equivalent inclusions introduced in the proposed model are ellipsoidal. Note that in the homogenization theory, ellipsoidal inclusions represent mechanical zones of influence rather than actual minerals or cracks (hence, the shape of cracks and biotite minerals does not need to be ellipsoidal to assume ellipsoidal inclusion shapes).

Here, we introduce the governing equations underlying the model. All the following notations are summarized in a table at the end of this paper. N_c is the number of crack inclusion types types (also called crack phases) in the REV. Here, we consider $N_c = 74$ crack phases which correspond to $N_c = 74$ different possible crack orientations. N_b is the number of biotite inclusion phases in the REV. Here, we consider $0 \le N_b \le 74$ biotite phases that also correspond to differences in biotite orientation (as opposed, for instance, to differences in weathering state). N is the number of phases in the REV: $N = N_c + N_b + 1$, where the matrix counts for one phase. Note that in comparison to our previous model (Shen et al., 2019), in which damage was an isotropic variable introduced to measure the degradation of the matrix stiffness, the representation of the microstructure proposed here is more realistic, because micro-cracks are modeled explicitly so as to represent all possible directions of crack propagation in the REV.

Equivalent inclusions of a phase undergo the same stress and strain fields (and the same eigenstress and eigenstrain fields). The local stress field of the *i*th phase is:

$$\sigma_{i} = \mathbb{C}_{i} : (\epsilon_{i} - \eta_{i}) = \mathbb{C}_{i} : \epsilon_{i} + \underbrace{(-\mathbb{C}_{i} : \eta_{i})}_{\pi_{i}}$$

$$\tag{9}$$

where σ_i , \mathbb{C}_i , ϵ_i , η_i , and π_i denote respectively the microscopic stress tensor, elastic stiffness tensor, strain tensor, uniform eigenstrain field and corresponding eigenstress field of the *i*th phase. The eigenstrain and eigenstress fields are zero in the crack and matrix phases.

The REV is subjected at its boundary to the macrostrain E and within its volume to the eigenstrain fields η_i . Thus, the microscopic strain tensor ϵ_i reads as (Pichler & Hellmich, 2010):

$$\epsilon_i = \mathbb{A}_i : E + \sum_{j=1}^N \mathbb{D}_{ij} : \eta_j$$
 (10)

In the equation above, the fourth-order strain concentration tensor \mathbb{A} establishes a linear relation between the microscopic strain field ϵ_i and the macroscopic one E. In the second term, \mathbb{D}_{ij} is the so-called influence tensor, which is used to model the effect of the eigenstrain of the jth phase η_j on the microscopic strain field of ith phase. The strain concentration tensor \mathbb{A}_i can be calculated as follows (Dormieux et al., 2006):

$$\mathbb{A}_i = \mathbb{A}_i^o : \left(\sum_{j=1}^N f_j \mathbb{A}_j^o\right)^{-1} \tag{11}$$

in which f_i is the volume fraction of the *j*th phase in the REV, and:

XU ET AL. 5 of 37

$$\mathbb{A}_{i}^{o} = [\mathbb{I} + \mathbb{P}_{i} : \delta \mathbb{C}_{i}]^{-1} \tag{12}$$

where $\delta \mathbb{C}_i = \mathbb{C}_i - \mathbb{C}^m$ (\mathbb{C}^m being the stiffness tensor of the matrix). In the equation above, \mathbb{A}_i^o relates the strain E_0 applied at the far-field boundary of the REV to the phase strain ϵ_i . \mathbb{P}_i is the Hill polarization tensor of the *i*th phase and represents how the micro-displacement field in that phase influences the micro-displacement fields in the other phases of the REV. The expression of the polarization tensor is explained in detail in Appendix A.

The explicit expression of the influence tensor \mathbb{D}_{ij} was given by Pichler and Hellmich (2010) as follows:

$$\mathbb{D}_{ij} = \left\{ \left[\delta_{ij} \mathbb{I} - f_j \mathbb{A}_i \right] : \mathbb{A}_j^o : \mathbb{P}_j \right. \\
+ \left[\mathbb{A}_i : \left\langle \mathbb{A}^o : \mathbb{P} \right\rangle - \mathbb{A}_i^o : \mathbb{P}_i \right] : \left\langle \left(\mathbb{C}^{\text{hom}} - \mathbb{C} \right) : \mathbb{A}^o : \mathbb{P} \right\rangle^{-1} : \\
f_j : \left[\left(\mathbb{I} - \mathbb{A}_j \right)^T + \left(\mathbb{C}^{\text{hom}} - \mathbb{C}_j \right) : \mathbb{A}_j^o : \mathbb{P}_j \right] \right\} : \mathbb{C}_j$$
(13)

Here \mathbb{C}^{hom} is the homogenized stiffness tensor of the REV. $\langle ... \rangle$ stands for the average over the volume of the REV (V_{REV}) . For example, for a generic continuous function of space $h\left(\underline{x}\right)$, the average value of h within the REV is:

$$\langle h\left(\underline{x}\right)\rangle = \frac{1}{V_{REV}} \int_{V_{REV}} h\left(\underline{x}\right) d\underline{x} \tag{14}$$

Similarly, if $h(\underline{x})$ is defined over a discrete set of N phases in the REV, then its average value over the REV is:

$$\langle h\left(\underline{x}\right)\rangle = \sum_{i=1}^{N} f_i h_i$$
 (15)

in which h_i designates the value of h in the inclusions of the ith phase (in which spatial functions are uniform), and f_i is the volume fraction of the ith phase in the REV.

2.2. Two-Step Homogenization

Our goal is to develop a two-step homogenization scheme to understand the interaction between the expansion of biotite inclusions due to weathering and the propagation of cracks in the matrix. The homogenization operation will not only provide the microscopic stress and strain fields, but also the crack densities in the N_c crack directions considered, the resulting damage (defined as a crack density tensor) and the corresponding macroscopic damaged stiffness tensor, which will be needed to investigate the effect of weathering at scales larger than that of the REV (in Sections 5 and 6).

Microscopic stresses are statically admissible with the macroscopic stress. Therefore, we can apply Levin's theorem (Laws, 1973), which states that the REV stress Σ can be calculated as the spatial average of the microscopic stresses. This leads to an expression that relates Σ to the REV strain E and the eigenstress π , as follows:

$$\Sigma = \mathbb{C}^{\text{hom}} : E + \langle \pi : \mathbb{A} \rangle \tag{16}$$

in which the homogenized stiffness tensor is:

$$\mathbb{C}^{\text{hom}} = \langle \mathbb{C} : \mathbb{A} \rangle \tag{17}$$

We conduct a two-step homogenization (Dai et al., 1998; Desrumaux et al., 2001; Meraghni et al., 2002) to calculate the REV stiffness tensor \mathbb{C}^{hom} (Figure 2). In step 1, we calculate the stiffness tensor of a set of cracks of 74 possible orientations embedded in an isotropic matrix. In step 2, we calculate the REV stiffness tensor as that of a set of biotite inclusions embedded in an anisotropic matrix that has the stiffness tensor calculated in step 1. The interaction between the biotite and crack inclusions is modeled through the new damaged matrix in step 2. Note that this two-step approach requires a separation of scale between the size of the cracks and that of the biotite minerals, that is, we assume that the micro-crack lengths are one to two orders of magnitude smaller than the longest dimension of the biotite inclusions. This is a realistic assumption, because the size of single biotite crystal is around 1 mm while the crack length in the matrix is around 0.1 mm (Nasseri et al., 2007). The stiffness tensors obtained after step 1 and after step 2 are symmetric because the Mori-Tanaka scheme yields unconditionally

XU ET AL. 6 of 37

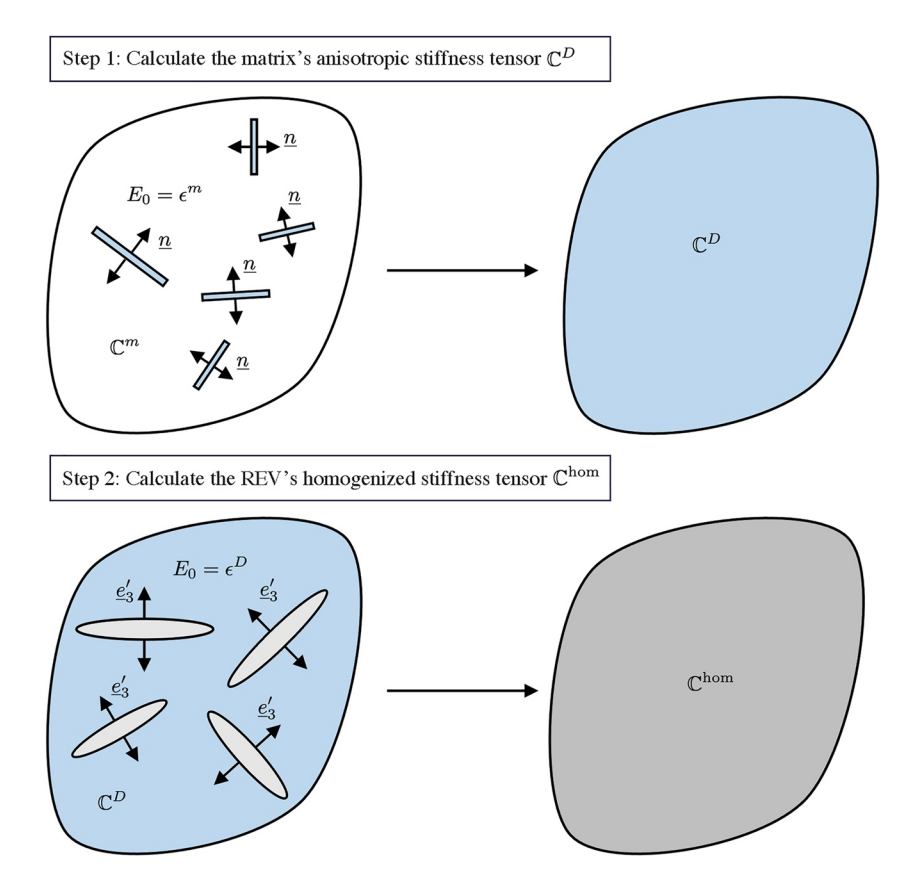


Figure 2. Schematic of the two-step approach to calculate the homogenized Representative Elementary Volume stiffness tensor \mathbb{C}^{hom} . Step 1: Calculate the stiffness of a set of cracks embedded in an isotropic matrix. \mathbb{C}^m represents the isotropic stiffness tensor of the matrix, and e^m represents the average strain field in the matrix. \mathbf{E}_0 is the far field strain, which, in the Mori-Tanaka scheme, is equal to $e^m \cdot \underline{n}$ represents the direction of crack opening. Cracks are oblate spheroids and \underline{n} is orthogonal to the plane of the two larger dimensions. Step 2: Calculate the stiffness of a set of biotite inclusions embedded in a damaged matrix that has the homogenized properties calculated in step 1. \mathbb{C}^D represents the anisotropic stiffness tensor of damaged matrix, and e^D represents the average strain field in the damaged matrix. \underline{e}_3' is the biotite expansion direction in the local coordinate system attached to the biotite inclusion.

symmetric homogenized stiffness tensors in two-phase systems (Benveniste et al., 1991; Chen et al., 1992). Thus, the proposed two-step homogenization procedure yields a symmetric REV stiffness tensor. The calculation of the stiffness tensor of the REV is based on more physical grounds than in our previous model (Shen et al., 2019), in which the damaged stiffness tensor of the matrix was updated with the value of a damage measure calculated based upon a phenomenological evolution law, as opposed to the actual propagation of micro-cracks.

In the following, the volume fractions of the matrix, biotite inclusions of kth orientation and crack inclusions of rth orientation are denoted f^n , f_b^k and f_c^r , respectively. Using Equation 17, the homogenized stiffness tensor \mathbb{C}^D of the crack-matrix system in the first homogenization step is calculated as the volume average of the product of stiffness tensor and strain concentration tensor of each phase:

$$\mathbb{C}^{D} = \sum_{j \in \mathcal{C}, \mathcal{M}} f_{j} \mathbb{C}_{j} : \mathbb{A}_{j}
= \left[f^{m} \mathbb{C}^{m} + \sum_{r=1}^{N_{c}} f_{c}^{r} \mathbb{C}_{c}^{r} : (\mathbb{I} + \mathbb{P}_{c}^{r} : \delta \mathbb{C}_{c}^{r})^{-1} \right] :
\left[f^{m} \mathbb{I} + \sum_{r=1}^{N_{c}} f_{c}^{r} (\mathbb{I} + \mathbb{P}_{c}^{r} : \delta \mathbb{C}_{c}^{r})^{-1} \right]^{-1}$$
(18)

XU ET AL. 7 of 37



in which C and M refer to the group of crack inclusion phases and to the matrix phase, respectively. In step 2, the Mori-Tanaka stiffness tensor of the two-phase system made of biotite inclusions embedded in a damaged matrix can be written as:

$$\mathbb{C}^{\text{hom}} = \sum_{j \in B, D} f_j \mathbb{C}_j : \mathbb{A}'_j \\
= \left[f^D \mathbb{C}^D + \sum_{k=1}^{N_b} f_b^k \mathbb{C}_b^k : \left(\mathbb{I} + \mathbb{P}_b^{k,'} : \delta \mathbb{C}_b^{k,'} \right)^{-1} \right] : \\
\left[f^D \mathbb{I} + \sum_{k=1}^{N_b} f_b^k \left(\mathbb{I} + \mathbb{P}_b^{k,'} : \delta \mathbb{C}_b^{k,'} \right)^{-1} \right]^{-1}$$
(19)

in which \mathcal{B} and \mathcal{D} represent the groups of biotite inclusion families and the damaged matrix that has the properties calculated in step 1, respectively. The 'superscript refers to the damaged matrix. The Hill polarization tensors $\mathbb{P}_b^{k,'}$ and the concentration tensors \mathbb{A}_j' (Equation 11) for the damaged matrix can be calculated by replacing \mathbb{C}^m by the damaged stiffness tensor \mathbb{C}^D in Equation A2.

The free energy of the REV, Ψ , is a function of the REV strain, E, and the crack density of rth crack phase, ρ^r . We compute Ψ by integrating Equation 16 as follows:

$$\Psi(E, \rho^{r}) = \frac{1}{2}E : \mathbb{C}^{\text{hom}}(\rho^{r}) : E + \sum_{i \in B, D} f_{i}(-\mathbb{C}_{i} : \eta_{i}) : \mathbb{A}'_{i}(\rho^{r}) : E$$

$$-\frac{1}{2} \sum_{i,j \in B, D} f_{i} \pi_{i} : \mathbb{D}_{ij}(\rho^{r}) : \mathbb{C}_{j}^{-1} : \pi_{j}$$
(20)

The first term on the right side of the equation above, $\frac{1}{2}E:\mathbb{C}^{\text{hom}}(\rho^r):E$, represents the deformation energy of the damaged REV. The second term, $\sum_{i\in B,D} f_i\left(-\mathbb{C}_i:\eta_i\right):\mathbb{A}_i'(\rho^r):E$, reflects the influence of the eigenstress that builds up in the biotite inclusions. The third term, $-\frac{1}{2}\sum_{i,j\in B,D} f_i\pi_i:\frac{\partial \mathbb{D}_{ij}}{\partial \rho^r}:\mathbb{C}_j^{-1}:\pi_j$, is a coupling term that reflects the inter-dependence between the macroscopic strain and the biotite eigenstress. This is substantially more complex than a linear elastic model, in which the expression of the free energy would only contain the first term, and in that term, the stiffness tensor of the REV, \mathbb{C}^{hom} , would be constant instead of being a function of the crack densities ρ^r .

Thermodynamic conjugation relationships define stress-like variables as the derivative of the free energy by the strain-like variables that are work-conjugate to these stress-like variables. Using thermodynamic conjugation relationships, we thus get:

$$\begin{cases} \mathbf{\Sigma} = \frac{\partial \Psi}{\partial \mathbf{E}} \\ f_i \boldsymbol{\epsilon}_i = \frac{\partial \Psi}{\partial \boldsymbol{\pi}_i} \end{cases}$$
 (21)

The first of the two equations above provides the expression of the macroscopic stress as given in Equation 16, and the second equation provides a relationship between the local strains and the local eigenstresses, which is similar to a porosity-pore pressure relationship in poromechanics (Dormieux et al., 2006; Pichler & Hellmich, 2010).

This section has provided the equations that are necessary to calculate the REV stress, strain and stiffness from the crack densities in the matrix and the microscopic stresses ad strains in the matrix, cracks and biotite inclusions. The calculation process is based on a two-step Mori-Tanaka homogenization scheme. One last ingredient is needed to close the formulation: the constitutive equations that govern the behavior of the inclusions (cracks and biotite inclusions). This is the object of Section 3.

XU ET AL. 8 of 37



3. Mechanical Processes: Coupling Biotite Weathering and Crack Propagation

To understand how the development of microcracks affects the stiffness of the REV, it is necessary to express the homogenized stiffness tensor \mathbb{C}^D (Equation 18) in terms of the characteristics of the open microcracks and closed microcracks. That is our goal in Sections 3.1–3.3. Section 3.4 explains how to calculate the eigenstrain η_i of the biotite inclusions (Equation 20), which is necessary to calculate the stiffness \mathbb{C}^{hom} of the REV.

3.1. Geometric Representation of Microcrack Inclusions

In this study, we represent microcracks as oblate spheroidal equivalent inclusions in the Mori-Tanaka scheme. A family of microcracks of same orientation can be characterized by a normal vector \underline{n} , which is oriented in the direction orthogonal to the plane formed by the two longer axes of the oblate spheroids. The two longer axes have dimension a, and we define c as the half opening of the cracks in the direction of the smaller axis. The aspect ratio X = c/a has to satisfy the condition $X \ll 1$ for the cracks to be considered "penny-shaped."

We consider 74 types of crack inclusions, which can be viewed as 74 families of cracks, each characterized by a distinct orientation and distinct initial dimensions. All cracks in a family are subject to the same local stresses and hence all have the same crack radius at any given time. Noting \underline{n}^r the vector normal to cracks of phase r, the crack density tensor of the rth crack phase is defined as $\rho^r \underline{n}^r \otimes \underline{n}^r$, where ρ^r is the crack density variable defined in mechanics (as will be explained below). At REV scale, the deformation induced by the micro-cracks is calculated as the integral of the crack density tensors over the unit sphere, to represent all possible crack orientations. Here, we approximate this integration by a summation of displacement jumps induced by a discrete distribution of 2×37 microplanes with normal direction \underline{n}^r and weight w^r (Bažant & Oh, 1986). The volume fraction f_c^r of cracks of orientation r (with radius a^r and aspect ratio $X^r = c^r/a^r$) can be expressed as follows:

$$f_c^r = \frac{4}{3}\pi \mathcal{N}^r \times (a^r)^3 \times X^r = \frac{4}{3}\pi \rho^r X^r$$
 (22)

where \mathcal{N}^r denotes the number of cracks per unit volume in the considered set, and $\rho^r = \mathcal{N}^r(a^r)^3$ is the crack density variable as defined in fracture mechanics for the *r*th family of cracks (Kachanov, 1992), which can be understood as the fraction of the REV that is influenced by the stress and strain fields of the *r*th family of cracks.

We define the second-order damage tensor Ω as:

$$\mathbf{\Omega} = \sum_{i=1}^{N_c} \rho^r \underline{n}^r \otimes \underline{n}^r \tag{23}$$

where $N_c=74$ is the number of crack families considered. The damage tensor can be viewed as a crack density tensor and this is one of the quantities that we focus on the most in this study. In the sum above, $\rho^r\underline{n}^r\otimes\underline{n}^r$ represents the elementary crack density tensor for rth family of cracks, which can be understood as a normal deformation in direction \underline{n}^r . Ω has nine components in a three-dimensional space. By construction, Ω is symmetric. We will be presenting components of the damage tensor in our simulations later in the manuscript, so it is useful to understand the meaning of these components here. In a coordinate system $(\underline{x},\underline{y},\underline{z})$, Ω_{xx} , Ω_{yy} and Ω_{zz} can be understood as a deformation induced by crack opening in directions x, y and z. For example, if cracks open in mode I, Ω_{xx} is a deformation induced by the opening of cracks of normal $\underline{n}=\underline{e}_x$ and by the projection in direction x of the opening displacement vectors of the cracks that have a normal vector different from \underline{e}_x . If cracks propagate in mode II, then Ω_{xy} is a pseudo deformation induced by cracks of normal \underline{e}_x in direction \underline{e}_y (and the projection of the deformation in direction y due to the cracks of normal $\underline{n}\neq\underline{e}_x$ in direction \underline{e}_x). Lastly, Ω is sometimes expressed in a principal base noted $(\underline{e}_1,\underline{e}_2,\underline{e}_3)$. In that case, the damage tensor is diagonal and the coefficients Ω_1 , Ω_2 and Ω_3 are the principal values of the damage tensor, which represent deformations in directions 1, 2, and 3 due to cracks of normal directions \underline{e}_1 , \underline{e}_2 and \underline{e}_3 , or their projections.

At a given time, cracks are expected to be open in some directions and closed in others. Here we let the subscripts cl and o refer to the closed cracks and the opened cracks, respectively. The stiffness tensor of open cracks is $\mathbb{C}^o_c = 0$, because there is no local stress on crack surfaces. We assume that the two faces of closed cracks are in frictionless contact. This means that a closed crack transmits the normal compression forces, whereas the shear

XU ET AL. 9 of 37



stress in the crack plane remains equal to 0. The closed cracks are viewed as flat inclusions filled by a fictitious linear elastic isotropic material of bulk modulus $k^c \neq 0$ and shear modulus $\mu^c = 0$, that is, $\mathbb{C}_c^{cl} = 3k^c \mathbb{J}$, where \mathbb{J} is the hydrostatic projection tensor defined in Equation 6.

Here, we use a fracture mechanics-based approach proposed by other authors to calculate the macroscopic properties of the cracked REV in step 1 (Deudé et al., 2002). Since cracks are penny-shaped, their aspect ratio X = c/a tends to zero. Therefore, the volume fraction of cracks in the *r*th direction is $f_c^r = 4\pi \rho^r X^r/3$ and tends to zero as well. By contrast, $f_c^r(\mathbb{I} + \mathbb{P}_c : \delta \mathbb{C}_c^r)^{-1}$ tends to $4\pi \rho^r \mathbb{T}^r/3$, in which the tensor \mathbb{T}^r is a finite limit defined by $X(\mathbb{I} - \mathbb{S})$, where \mathbb{S} is Eshelby tensor. For open cracks, \mathbb{T}^r is:

$$\mathbb{T} = \frac{4(1 - \nu^{s})}{\pi} \left(\frac{\nu^{s}}{1 - 2\nu^{s}} \underline{n} \otimes \underline{n} \otimes \underline{I} \right)
+ \frac{1}{1 - \nu^{s}} \left(\underline{I} \otimes \underline{n} \otimes \underline{n} + \underline{n} \otimes \underline{n} \otimes \underline{I} \right) - \frac{\nu^{s}}{2 - \nu^{s}} \underline{n} \otimes \underline{n} \otimes \underline{n} \otimes \underline{n} \otimes \underline{n} \right)$$
(24)

For closed cracks, \mathbb{T}^r is (Dormieux et al., 2006):

$$\mathbb{T}' = \frac{4(1 - v^s)}{\pi (2 - v^s)} \left(I \underline{\overline{\otimes}} \left(\underline{n} \otimes \underline{n} \right) + \left(\underline{n} \otimes \underline{n} \right) \underline{\overline{\otimes}} I - 2 \left(\underline{n} \otimes \underline{n} \right) \otimes \left(\underline{n} \otimes \underline{n} \right) \right)$$
(25)

Therefore, the homogenized stiffness tensor given in Equation 18 can be expressed as (Dormieux & Kondo, 2009):

$$\mathbb{C}^{D} = f^{m}\mathbb{C}^{m} : \left(f^{m}\mathbb{I} + \sum_{r \in \mathcal{C}} \frac{4\pi\rho^{r}}{3}\mathbb{T}^{r}\right)^{-1}$$

$$= f^{m}\mathbb{C}^{m} : \left(f^{m}\mathbb{I} + \sum_{r \in \mathcal{O}} \frac{4\pi\rho^{r}}{3}\mathbb{T}^{r} + \sum_{r \in \mathcal{CL}} \frac{4\pi\rho^{r}}{3}\mathbb{T}^{\prime,r}\right)^{-1}$$
(26)

in which C, O and CL respectively refer to all the crack phases (or orientations), the open crack phases (orientations) and the closed crack phases (orientations). At this point in the model, all the terms in the equation above can be expressed explicitly, which is in contrast with Equation 18. The explicit expression of \mathbb{C}^D in Equation 26 is useful for the calculation of the derivatives of damage stiffness tensor in the next section.

3.2. Microcrack Propagation and Evolution

The "force" \mathcal{G}_{ρ}^{r} that drives crack propagation is thermodynamically conjugated to the crack density ρ^{r} , and is calculated as the negative partial derivative of the strain energy of the REV, Ψ , with respect to the crack density ρ^{r} .

$$\mathcal{G}_{\rho}^{r} = -\frac{\partial \Psi\left(E, \rho^{r}\right)}{\partial \rho^{r}} \\
= -\frac{1}{2}E : \frac{\partial \mathbb{C}^{\text{hom}}}{\partial \rho^{r}} : E + \sum_{i \in B, D} f_{i} \boldsymbol{\pi}_{i} : \frac{\partial \mathbb{A}_{i}^{\prime}}{\partial \rho^{r}} : E - \frac{1}{2} \sum_{i, j \in B, D} f_{i} \boldsymbol{\pi}_{i} : \frac{\partial \mathbb{D}_{ij}}{\partial \rho^{r}} : \mathbb{C}_{j}^{-1} : \boldsymbol{\pi}_{j}$$
(27)

 G_{ρ}^{r} represents the so-called damage driving force associated with the rth family of microcracks. The explicit expression of G_{ρ}^{r} is derived in Appendixes B and C. The damage criterion g is a function of the force that drives crack propagation, G_{ρ} , and the crack density ρ^{r} . For each crack orientation r (which can take values between 1 and N_{c}), it is written as:

$$g(\mathcal{G}_{\varrho}^{r}, \rho^{r}) = \mathcal{G}_{\varrho}^{r} - \mathcal{R}^{r} \ge 0 \tag{28}$$

in which \mathcal{R}^r represents the material's resistance to damage. In order to account for material softening with a minimum number of parameters, we propose to use the following exponential function:

$$\mathcal{R}^r = R_c \, \xi^r \exp(1 - \xi^r) \tag{29}$$

with $\xi^r = \rho^r/\rho_c$, in which ρ_c represents a critical crack density. The function \mathcal{R}^r increases when $\rho^r \leq \rho_c$ to account for strain hardening, and decreases when when $\rho^r > \rho_c$ to describe strain softening. R_c is the maximal value of \mathcal{R}^r , attained at $\rho = \rho_c$. A graphical representation of \mathcal{R}^r is shown in Figure 3.

XU ET AL. 10 of 37



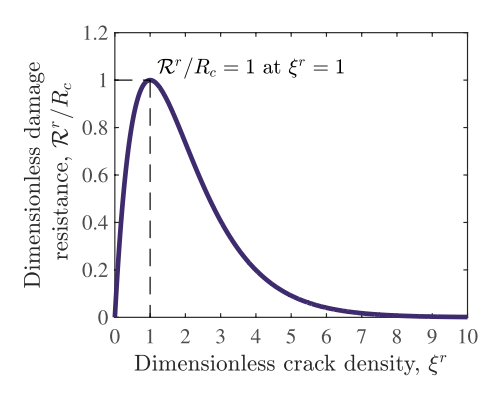


Figure 3. Dependence of the dimensionless crack propagation criterion \mathcal{R}^r/R_c on the dimensionless crack density $\xi^r = \rho^r/\rho_c$. The resistance to damage \mathcal{R}^r reaches a maximum value R_c at $\xi^r = 1$.

3.3. Microcrack Closure

The stiffness tensor of a crack, \mathbb{C}_c , is either the null tensor (if the crack is open), or $3k^c\mathbb{J}$ (if the crack is closed). To choose the appropriate tensor for each crack inclusion phase, we establish a crack opening-closure transition condition, explained in the following. The local strain rate can be obtained by taking the time derivative of Equation 10.

$$\dot{\boldsymbol{\epsilon}}^r = \mathbb{A}^r : \dot{\boldsymbol{E}} + \sum_{k=1}^{N_b} \mathbb{D}_{rb}^k : \dot{\boldsymbol{\eta}}^{b,k}$$
 (30)

Here the index k refers to the kth biotite orientation represented in the REV. Note that the only eigenstrains involved in the equation above are those of the biotite inclusions, which can expand due to weathering. The cracks and the matrix are not endowed with any eigenstrain. Cracks close when the rate of change of crack width is negative (i.e., at $\dot{c}^r < 0$). We have:

$$\dot{c}^r = c^r n \cdot \dot{e}^r \cdot n \tag{31}$$

Defining the initial state as a state of zero strain, the cumulative change in crack width from the initial state is:

$$\delta c^r = c^r n \cdot (\mathbb{A}^r : E + \mathbb{D}_{rb} : \eta^b) \cdot n \tag{32}$$

It is thus convenient to use the variable δc^r as an indicator for the crack opening-closure transition criterion in the rth family. Crack closure is completed when the crack width reaches zero (i.e., at $\delta c^r = -c_0^r$, in which c_0^r stands for the value of c^r in the initial state).

3.4. Mineral Inclusion Subject to Weathering

To model the eigenstrains of minerals subject to weathering, we use a model proposed by the authors (Shen et al., 2019) at the scale of a single biotite crystal (\sim 1 mm). Inclusions are represented as oblate spheroids. In order to account for the layered structure of biotite, chemical weathering is assumed to drive expansion only in the direction of the spheroid thickness (noted $\underline{e_3}'$). We denote $V_{\text{b,initial}}$ as the initial volume of non-weathered biotite in the mineral inclusion, V_b^w the weathered biotite volume in the inclusion at time t, and V_b the remaining unweathered biotite volume in the inclusion at time t. Because a layer of biotite dilates by a factor of 1.4 during the weathering step when potassium cations are replaced by hydrated magnesium cations (Shen et al., 2019), at time t the unweathered biotite volume can be written as $V_b = V_{b,\text{initial}} - V_b^w / 1.4$. In this study, we refer to the strain induced by chemical weathering of biotite as the chemical strain. The chemical strain in the thickness direction is thus calculated as:

$$\eta_b^c = \frac{V_b^w + V_b}{V_{b,\text{initial}}} - 1 = \frac{V_b^w \left(1 - \frac{1}{1.4}\right)}{V_{b,\text{initial}}}$$
(33)

It was shown that the rate of change of the volume of weathered biotite can be expressed as (Shen et al., 2019):

$$\frac{dV_b^w}{dt} = v_m \frac{dQ}{dt} \tag{34}$$

where $v_{\rm m}$ is the molar volume of weathered biotite ($v_{\rm m} = 2.10e-4~{\rm m}^3/{\rm mol}$) and Q is the number of moles of weathered biotite in the REV. The production rate of weathered biotite within the REV (${\rm d}Q/{\rm d}t$) can be expressed as:

$$\frac{dQ}{dt} = RS \tag{35}$$

in which R is the chemical weathering rate of biotite per unit mineral surface area and S is the total biotite surface area within the REV. We follow White and Brantley (2003) in adopting the following empirical model of biotite chemical weathering rate:

XU ET AL. 11 of 37



Table 1 Model Parameters		
Elastic moduli		
Material	Bulk modulus (MPa)	Shear modulus (MPa)
Biotite	76,700	41,600
Vermiculite	13,824	5,300
Matrix	60,700	31,300
Initial crack density	Damage parameters	
$\rho^{r,0}$	$ ho_{ m c}$	R _c (MPa)
1.25 <i>e</i> -6	1	5

$$R = 10^{-12.32} t^{-0.603} (36)$$

in which the time (t) is the time since the onset of weathering, expressed in years.

4. Simulation of Anisotropic Damage Propagation Under Various Stress and Weathering Conditions

In this section, we analyze the sensitivity of the micro-macro model to the loading conditions, the microscopic crack evolution parameters (also called damage parameters) and the orientation of the biotite inclusions. We consider a REV that contains 74 families of crack inclusions with different orientations but the same initial size a_0/c_0 (and therefore the same initial crack density variable ρ^0 , and only one family of biotite inclusions, such that the biotite inclusions are all aligned: $N_b=1$). These initial conditions result in an isotropic initial damage tensor (Equation 23): $\Omega^0_1=\Omega^0_2=\Omega^0_3=\Omega^0$.

The simulations that follow aim to understand whether biotite expansion can induce crack propagation under typical lithostatic conditions and to distinguish the most important components of the free energy that control crack propagation in Equation 20. These analyses at REV scale will allow us to interpret the finite element method (FEM) simulations for boundary value problems in Sections 5 and 6.

The tests that follow are conducted at the material point, that is, at REV scale. In each simulation, we consider that biotite inclusions have an initial volume fraction of 15% (which is typical of granites) and an initial aspect ratio of $a_b/c_b = 3$, where c_b is the thickness of the mineral, in direction \underline{e}'_3 (an aspect ratio of 3 is common for biotite minerals embedded in granite). The rock in these simulations starts from an unweathered state, that is, the initial eigenstrain is zero in the biotite inclusions. The baseline parameters used in the model for the following sensitivity analysis are listed in Table 1 and are taken from Nasseri et al. (2005) and Shen et al. (2019).

4.1. Numerical Algorithm

Simulations at the material point are conducted by means of two algorithms. The first one (Algorithm 1) detects the directions in which cracks are propagating. The second one (Algorithm 2) calculates the crack strains when cracks propagate, and updates the local strains and stresses in all phases.

In Algorithm 1, the damage criterion is checked for each crack set. If the criterion is reached in a crack set, that set is added to the so-called "trial active set." If the trial active set is empty, the homogenized stiffness tensor and strain concentration tensors at step n + 1 are identical to those at step n. If the trial active set is not empty, Algorithm 2 is triggered and the local stress and strain fields are solved iteratively with the Newton-Raphson method.

We then calculate crack opening displacements in the trial active set and check whether the crack closure is complete, that is, we check whether $c^{\alpha}=0$. If $c^{\alpha}=0$, closure is complete and we drop the α th crack set from the active set $\mathcal{J}^{(k)}_{\text{act},n+1}$, and we restart the local Newton-Raphson iteration by updating the homogenized stiffness tensor $\mathbb{C}^{\text{hom},(k+1)}_{n+1}$ and strain concentration tensor $\mathbb{A}^{(k+1)}_{l,n+1}$.

XU ET AL. 12 of 37

Algorithm 1. Predictor Phase

```
1 At integration point compute strain increment \Delta \epsilon_{n+1} and eigenstrain increment \Delta \eta_{n+1};
2 Compute the trial stress \Sigma_{n+1}^{\rm trial} = \mathbb{C}_n^{\rm hom} : E_{n+1} + \langle \pi_{n+1} : \mathbb{A}'_n \rangle;
3 Assemble trial active crack set \mathcal{J}_{\rm act,n+1}^{\rm trial} = \{\alpha \in \mathcal{O} \mid g_{n+1}^{r, {\rm trial}} > 0\};
4 if \mathcal{J}_{act,n+1}^{\rm trial} = \emptyset then
5 \mid \Sigma_{n+1} = \Sigma_{n+1}^{\rm trial};
6 \mid \mathcal{J}_{\rm act,n+1} = \mathcal{J}_{\rm act}^{\rm trial,n+1};
7 \mid \mathbb{C}_{n+1}^{\rm hom} = \mathbb{C}_n^{\rm hom};
8 \mid \mathbb{A}'_{i,n+1} = \mathbb{A}'_{i,n} Exit;
9 else
10 \mid \text{Call Algorithm 2};
11 \mid \text{Update } \mathbb{C}_{n+1}^{\rm hom}, \mathbb{A}'_{i,n+1}, \rho_{n+1}^{r} \text{ and } \mathcal{J}_{\rm act,n+1};
12 \mid \text{Exit};
13 end
```

4.2. Influence of Depth on REV Damage and Strain

In each of the following simulations, we impose an overburden stress σ_v . In the global orthonormal frame $(\underline{e}_1,\underline{e}_2,\underline{e}_3)$, we have $\sigma_v=\underline{e}_3\cdot\Sigma\cdot\underline{e}_3$, in which \underline{e}_3 is the vertical unit vector and \underline{e}_1 and \underline{e}_2 are the horizontal unit vectors (Figure 4). We follow Shen et al. (2019) in applying a lateral proportional stress boundary condition, such that the REV is constrained horizontally by a lateral boundary stress $\sigma_h=K\sigma_v$. We run simulations with K=0.5. The orientation of the aligned biotite inclusions is specified by three Euler angles, as illustrated in Figure 4. One begins with the biotite coordinate system in which the axes are parallel to those of the bedrock REV coordinate system (x_1,x_2,x_3) . The system is first rotated about the x_3 -axis through the angle ψ to the coordinate system (u,v,x_3) , and then rotated about the v-axis through the angle θ to the coordinate system (U,v,x_3') . Finally, the coordinate system of the aligned biotite inclusions (x_1',x_2',x_3') is obtained by a rotation about the x_3 -axis through the angle ϕ . The projection tensor from the global to the local frame is denoted \mathbf{R} and can be decomposed as follows (Bunge, 2013):

$$\mathbf{R} = \mathbf{R}_{\phi} \cdot \mathbf{R}_{\theta} \cdot \mathbf{R}_{\psi} \tag{37}$$

in which:

$$\begin{bmatrix} R_{\psi} \end{bmatrix} = \begin{bmatrix} \cos \psi & \sin \psi & 0 \\ -\sin \psi & \cos \psi & 0 \\ 0 & 0 & 1 \end{bmatrix} \begin{bmatrix} R_{\theta} \end{bmatrix} = \begin{bmatrix} \cos \theta & 0 & -\sin \theta \\ 0 & 1 & 0 \\ \sin \theta & 0 & \cos \theta \end{bmatrix} \begin{bmatrix} R_{\phi} \end{bmatrix} = \begin{bmatrix} \cos \phi & \sin \phi & 0 \\ -\sin \phi & \cos \phi & 0 \\ 0 & 0 & 1 \end{bmatrix}$$
(38)

The vector parallel to the thickness of the biotite inclusions (\underline{e}'_3) provides the direction of biotite expansion (Figure 4).

Our goal in these simulations is to show the effect of depth on the homogenized properties of the granite REV. We run these simulations under $\sigma_v = 0.0196$, 0.196, 1.96, and 19.6 MPa, corresponding to depths of h = 1, 10, 100 and 1,000 m with model parameters listed in Table 1. The orientation of the biotite inclusions is $(\psi, \theta, \phi) = (0, 0, 0)$ in all simulations (i.e., the biotite inclusions are horizontal, with \underline{e}'_3 parallel to \underline{e}_3). Figure 5 shows the results of REV scale simulations that investigate the influence of overburden stress σ_v on the REV volumetric strain, the normalized damage components $\overline{\Omega}_i$ (where the damage tensor Ω is defined in Equation 23 and the normalized damage components are scaled by initial damage value, Ω_0 , as $\overline{\Omega}_i = \Omega_i/\Omega_0$), and the normalized largest eigenvalue of stiffness tensor C_λ/C_λ^0 (where C_λ is the largest eigenvalue of homogenized stiffness tensor and C_λ^0 is the initial largest eigenvalue of elastic stiffness tensor).

Several observations emerge from the simulations in Figure 5. First, the bedrock accumulates less damage at greater depths (Figures 5a and 5b). This is because the larger overburden stresses at depth inhibit the growth of crack openings in the direction of biotite expansion (\underline{e}_3). As a result, volumetric expansion of the REV is larger at shallower depths, where the overburden compressive stresses are smaller (Figure 5c).

XU ET AL. 13 of 37

Algorithm 2. Determination of Active Crack Sets

```
1 Initialize the active set \mathcal{J}_{\mathrm{act},n+1}^{(0)} = \mathcal{J}_{\mathrm{act},n}^{\mathrm{trial}};
2 Set initial values of crack density: \rho_{n+1}^{r,(0)} = \rho_n^r;
3 Get the current energy release rate: \mathcal{G}_{\rho}^r from Eq. 27;
4 Compute the residuals for active crack sets (\alpha, \beta \in \mathcal{J}_{\mathrm{act},n+1}^{(k)}): r^{\alpha} = \mathcal{G}_{\rho}^{\alpha} - \mathcal{R}(\rho^{\alpha});
5 Construct the Jacobian: J^{\alpha\beta} = \partial_{\rho^{\beta}} \mathcal{G}_{\rho}^r - \partial_{\rho^{\beta}} \mathcal{R}(\rho^{\alpha});
6 Update incremental crack density: \rho^{\alpha,(k+1)} \leftarrow \rho^{\alpha,(k)} + \sum_{\alpha \in \mathcal{J}_{\mathrm{act},n+1}^{(k)}} (J^{-1})^{\alpha\beta} r^{\beta};
7 if (\sqrt{\sum_{\alpha \in \mathcal{J}_{\mathrm{act},n+1}^{(k)}} [r^{\alpha}]^2} > TOL) then
8 | Go to 3
9 end
10 if \delta c^{\alpha} = -c_0^{\alpha} \ \forall \ \alpha \in \mathcal{J}_{\mathrm{act},n+1}^{(k)} then
11 | \mathcal{J}_{\mathrm{act},n+1}^{(k+1)} \leftarrow \{\mathcal{J}_{\mathrm{act},n+1}^{(k)} \setminus \alpha\};
12 | Update \mathbb{C}_{n+1}^{\mathrm{hom},(k+1)}, \mathbb{A}_{i,n+1}^{(k+1)} and go to 2
13 else
14 | Construct the consistent tangent stiffness from Eq. D3
```

A second phenomenon that emerges from these simulations is a reduction in rock stiffness over time. As damage grows larger, the bedrock grows progressively less stiff and hence more deformable (Figure 5d).

The third behavior apparent in Figure 5 is that the REV experiences variations in volumetric strain over time. Volumetric strain is initially slightly compressive (negative) because of the overburden stress and the confining stress. As biotite inclusions expand, the rock becomes dilatant (Figure 5c).

A fourth observation is that damage propagates in all three directions, with larger damage components in the vertical direction, which correspond to projections of crack planes onto horizontal planes of normal vector \underline{e}_3 . This can be attributed to the vertical tensile stress induced by biotite expansion. Due to the axis-symmetry of the loading conditions and microstructure, damage is axis-symmetric (i.e., damage components in directions 1 and 2 are equal).

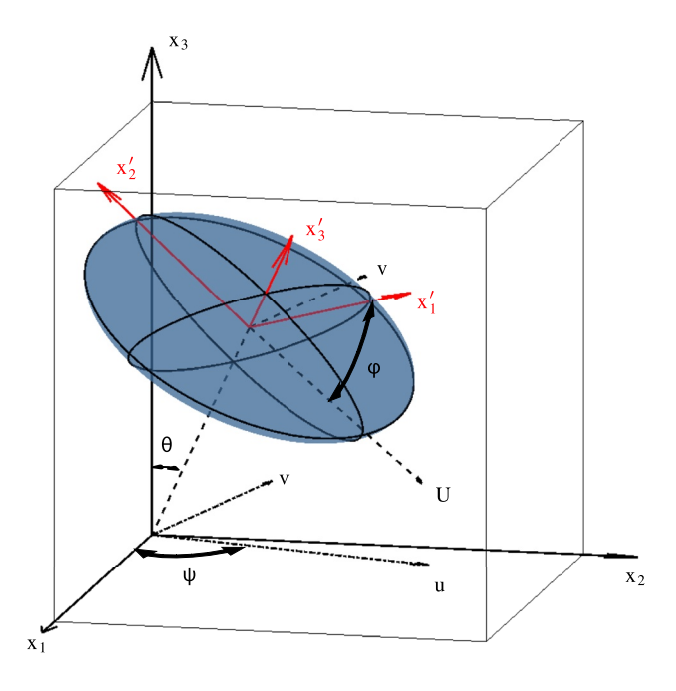


Figure 4. The local coordinate system of the ellipsoidal biotite inclusion. ψ , θ , and ϕ are the Euler angles, defining the orientation of the inclusion.

4.3. Influence of Damage Evolution Parameters on REV Damage and Strain

The criterion for damage propagation (i.e., crack opening growth) is governed by Equations 28 and 29, which depend on two important parameters: the critical crack density ρ_c , below which, the damaged material is hardening, and above which, the material is softening; and the maximum crack propagation threshold R_c , which is the maximum energy barrier that needs to be overcome in the loading history of the material, when it transitions between hardening and softening at $\rho = \rho_c$. Note that R_c is similar to a critical threshold at the scale of the rock matrix. At the scale of the REV though, micro-cracks may propagate at a lower stress than the granite strength. The model thus represents subcritical crack growth at the scale of the granite REV via a model of critical crack growth in the matrix and a homogenization of local stress fields. Figures 6 and 7 show the influence of ρ_c and R_c on the REV damage components and volumetric strains. We present results obtained under proportional loading with K = 0.5 at a depth of 30 m for R_c values of 0.5, 1, 2, and 3 MPa (each with $\rho_{\rm c}$ = 0.5), and for $\rho_{\rm c}$ values of 0.01, 0.05, 0.1, and 0.5 (each with $R_c = 3$ MPa). All simulations are conducted with horizontally oriented biotites (i.e., with $(\psi, \theta, \phi) = (0, 0, 0)$).

As expected from the definition of the model parameters, the damage evolution curves show that, for larger values of the critical crack density $\rho_{\rm c}$ and

XU ET AL. 14 of 37

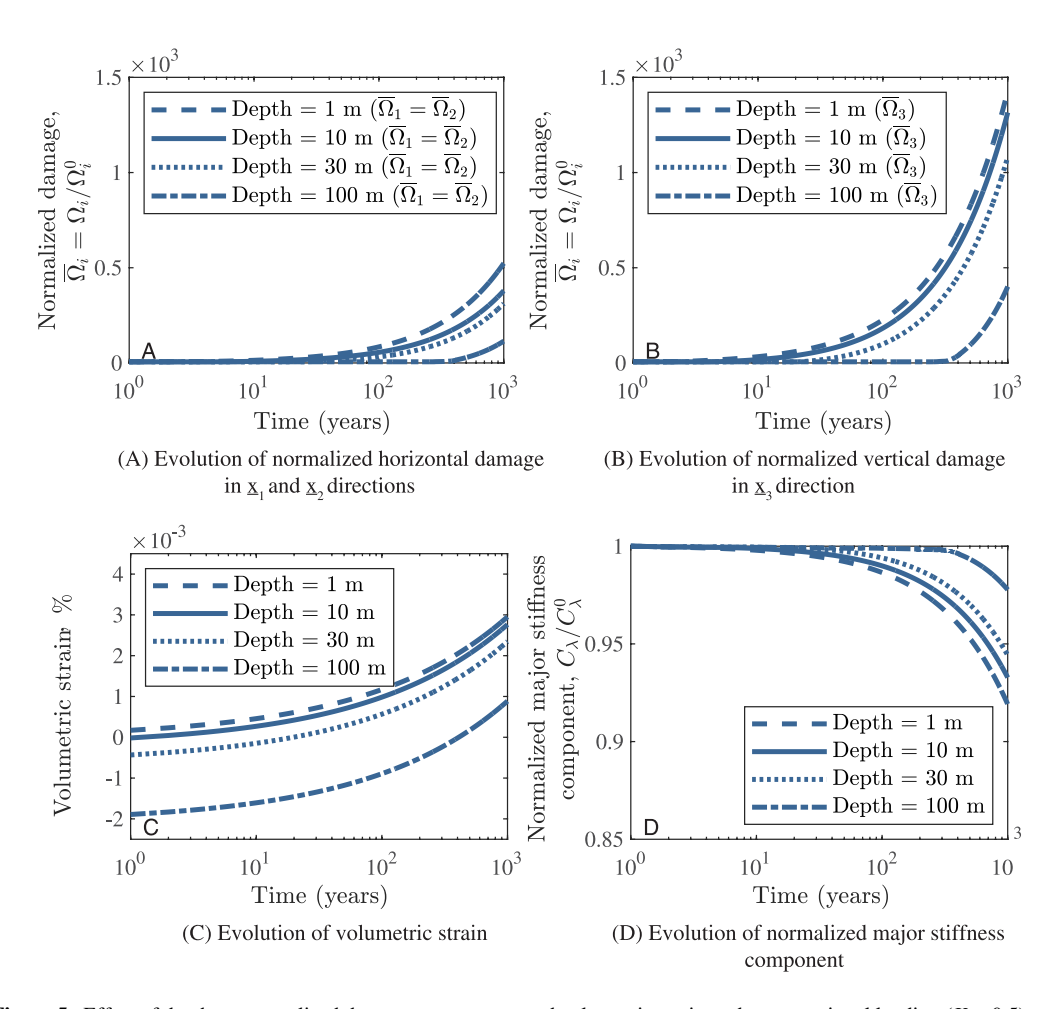


Figure 5. Effect of depth on normalized damage components and volumetric strain under proportional loading (K = 0.5). (a): Under proportional loading, the damage tensors are transverse isotropic for all depths $(\overline{\Omega}_1 = \overline{\Omega}_2)$. (b): The normalized damage component along \underline{x}_3 direction (projection of micro-cracks in the horizontal plane) is greater than that along the \underline{x}_1 and \underline{x}_2 directions (projection of micro-cracks in the vertical planes). Bedrock accumulates less damage at greater depths. (c): As biotite inclusions expand, the volumetric strain turns from compressive to dilative. Volumetric expansion is larger at shallower depths. (d): As damage accumulates, the material stiffness decreases over time.

smaller values of the minimum crack propagation threshold R_c , damage initiates earlier and more damage accumulates (Figures 6 and 7). At a given crack density ρ^r and a given value of R_c , the resistance to crack propagation \mathcal{R}^r is indeed larger for a lower ρ_c during the hardening regime. It means that it is harder to damage during the hardening regime when ρ_c is lower. Similarly, the expression of \mathcal{R}^r in Equation 29 indicates that the energy release needed to propagate damage increases with R_c . The trends in volumetric strains follow those of damage: the higher the damage, the higher the REV volumetric strain, and so, more volumetric strain accumulates when the critical crack density is high or when the critical propagation threshold is low.

Figure 8 shows the evolution of the three energy components that drive damage accumulation in Equation 27 for different sets of crack inclusions: crack planes orthogonal to the direction of biotite expansion (i.e., parallel to the biotite inclusions) with $\underline{n}/|\underline{e}'_3|$ (where // is the parallel operator), and crack planes parallel to the direction of biotite expansion, with $\underline{n}/|\underline{e}'_1|$. In both cases, the release of energy that dominates crack propagation is attributed to the eigenstress term $\sum_{i \in B,D} f_i \pi_i : \frac{\partial A'_i}{\partial \rho'} : E$ (Equation 20), which is up to 50% higher than macroscopic deformation energy term $-\frac{1}{2}E : \frac{\partial \mathbb{C}^{\text{hom}}}{\partial \rho'} : E$. The coupling term $-\frac{1}{2}\sum_{i,j \in B,D} f_i \pi_i : \frac{\partial \mathbb{D}_{ij}}{\partial \rho'} : \mathbb{C}_j^{-1} : \pi_j$, which translates the interdependence between macroscopic strains and biotite eigenstress, is negligible. All energy components are about eight times larger for cracks that open up in the direction of biotite expansion $(n/|\underline{e}'_3|)$.

XU ET AL. 15 of 37

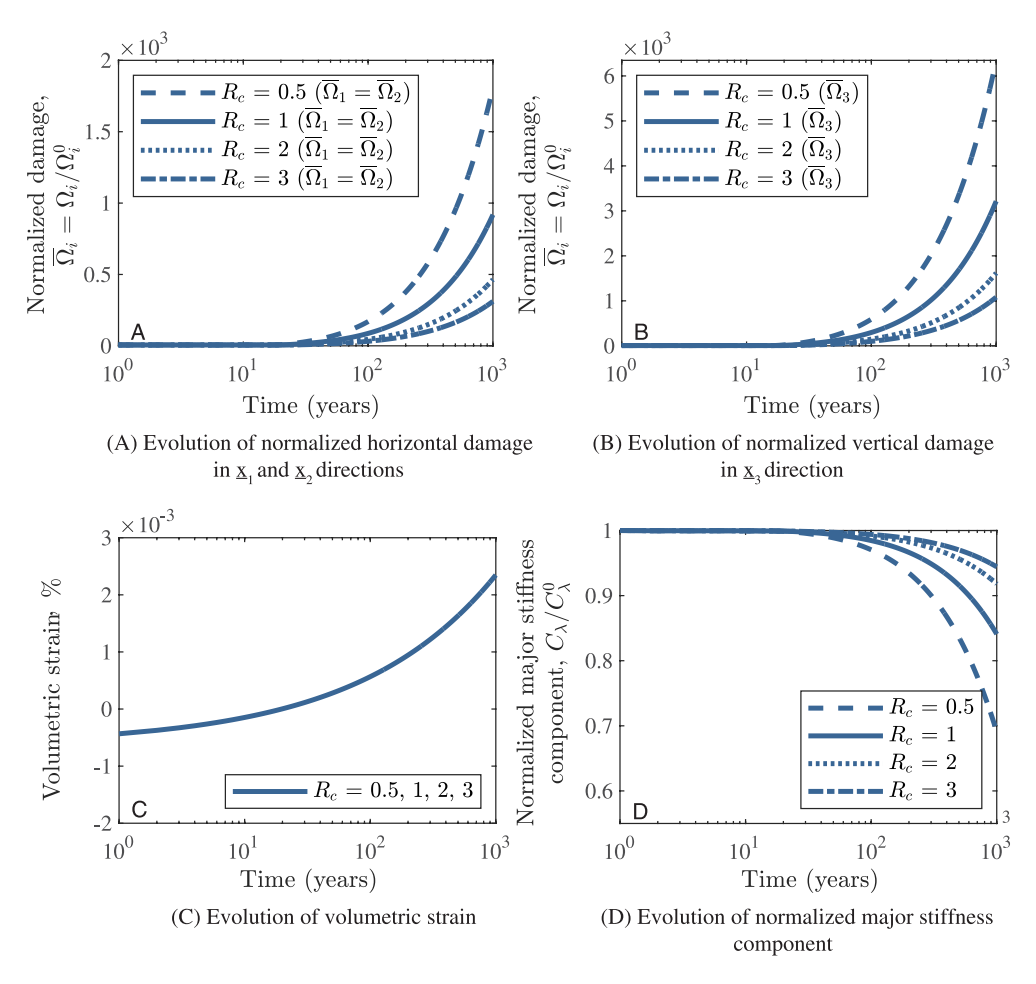


Figure 6. Effect of crack maximum propagation threshold R_c on normalized damage components and volumetric strain under proportional loading (K=0.5). (a): Under proportional loading, the damage tensors are transverse isotropic for all depths $\left(\overline{\Omega}_1=\overline{\Omega}_2\right)$. (b): The normalized damage component along direction \underline{x}_3 is greater than that along directions \underline{x}_1 and \underline{x}_2 . The damage initiates earlier and more damage accumulates for smaller values of the minimum crack propagation threshold R_c . (c): The volumetric strain evolution for different R_c values are indistinguishable within the width of the plotted line. (d): The stiffness decreases more with smaller R_c values.

4.4. Influence of Biotite Orientation on Damage

The model of bedrock presented here assumes that the REV contains aligned biotite minerals and randomly distributed sets of cracks that can have different densities (corresponding to more or less open cracks). As a result, the REV is assumed to be intrinsically anisotropic, that is, to exhibit an anisotropic mechanical behavior before weathering occurs. Note that the cracks are embedded in the matrix and are not necessarily following the biotite boundaries. Assuming a random distribution of crack orientations in the initial configuration allows us to explain damage anisotropy by regional, topographic and weathering stresses, and to correlate the orientations of propagated micro-cracks to the orientation of the biotite minerals. To better understand the influence of the orientation of the biotite minerals on the development of damage-induced anisotropy, we conducted simulations under proportional loading with K = 0.5 for a depth of 1,000 m, with the model parameters listed in Table 1, for which all crack orientations are initially equi-probable but the biotite inclusion orientation is different for every simulation. The projection of the biotite eigenstrains from the local to the global coordinate system is performed through the rotation matrix $\mathbf{R}^T = \mathbf{R}_{\psi}^T \cdot \mathbf{R}_{\phi}^T \cdot \mathbf{R}_{\phi}^T$, in which ψ , ψ , and ψ are the Euler angles. Note that since the biotite inclusions are oblate spheroids and expand in direction e_3 , the mechanical behavior of the REV does not vary with the angle ψ , which can be understood as a spin angle. We conducted simulations under 49 biotite orientations, for $\psi = (0, \pi/12, \pi/6, \pi/4, \pi/3, 5\pi/12, \pi/2)$, $\theta = (0, \pi/12, \pi/6, \pi/4, \pi/3, 5\pi/12, \pi/2)$ and $\phi = 0$.

XU ET AL. 16 of 37



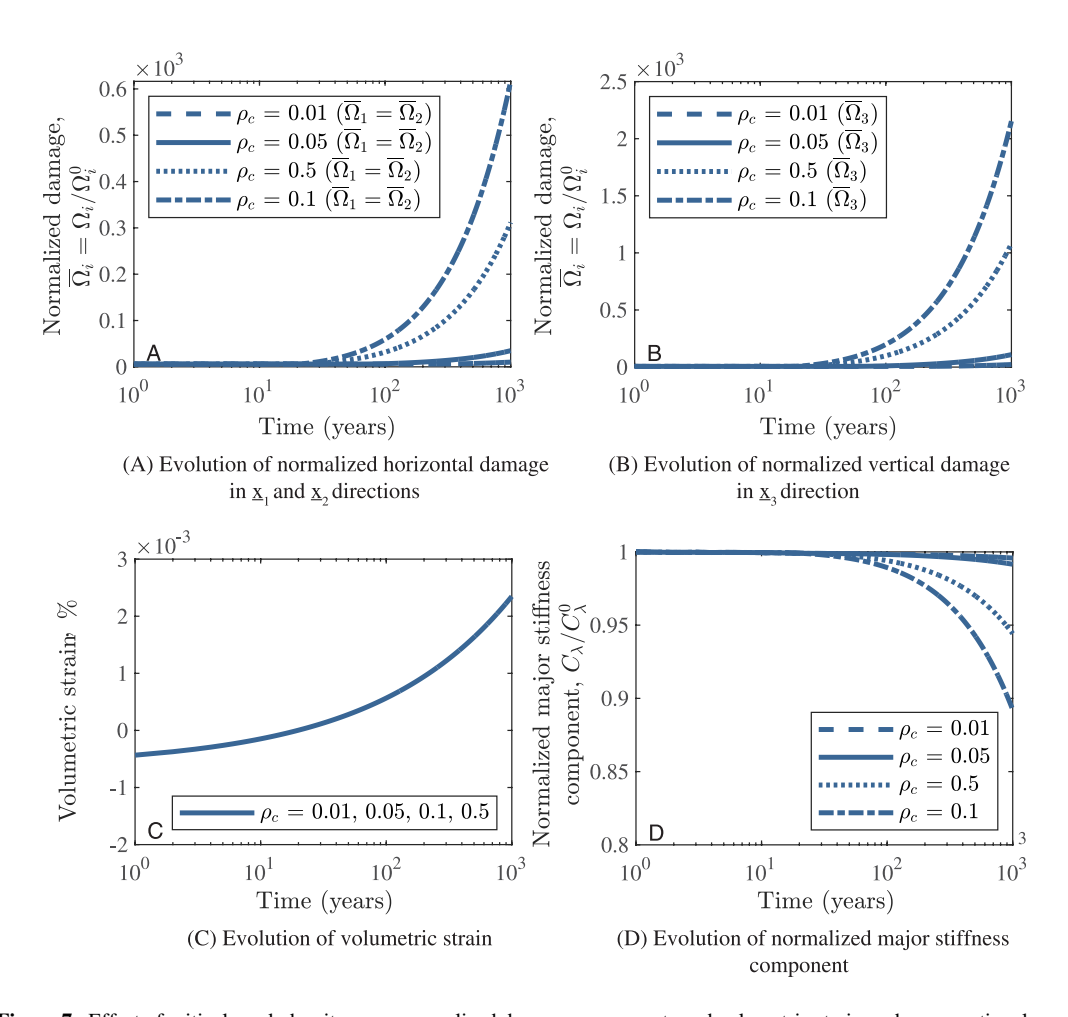


Figure 7. Effect of critical crack density ρ_c on normalized damage components and volumetric strain under proportional loading (K=0.5). (a): Under proportional loading, the damage tensors are transverse isotropic for all depths $(\overline{\Omega}_1=\overline{\Omega}_2)$. (b): The normalized damage component along direction \underline{x}_3 is greater than that along directions \underline{x}_1 and \underline{x}_2 . The damage initiates earlier and more damage accumulates for larger values of the critical crack density ρ_c . (c): The volumetric strain evolution for different ρ_c values are indistinguishable within the width of the plotted line. (d): A larger decrease of stiffness is observed for higher values of ρ_c .

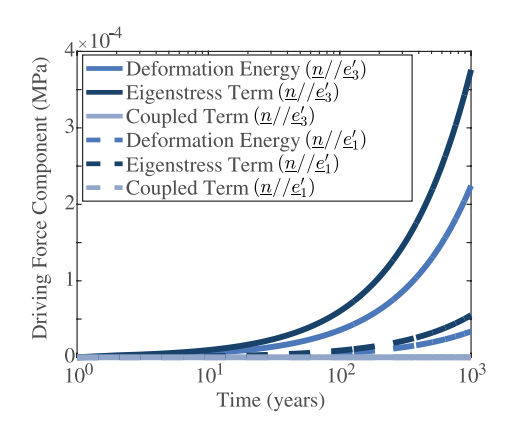


Figure 8. Driving force components (MPa) driving crack propagation in different directions (Equation 20). The eigenstress term dominates the evolution of damage driving force in both cases, indicating that biotite expansion is the dominant driver of crack propagation in these simulations.

Figure 9 shows the normalized damage components after a period of 1,000 years of weathering. We first note that when $\theta=0$, the local direction \underline{e}_3' of the biotite inclusion coincides with the vertical loading direction \underline{e}_3 . In addition, the imposed proportional loading condition results in triaxial compression, that is, $\Sigma_1=\Sigma_2$. Therefore, the mechanical behavior of the composite is symmetric about \underline{e}_3 , and the normalized damage components in the two horizontal principal directions one and two are identical (i.e., $\overline{\Omega}_1=\overline{\Omega}_2$), regardless of the value of ψ .

Biotite expansion induces anisotropy in damage and strain in the REV. To better understand this anisotropy, we define a scalar measure of the relative orientation of damage and loading directions:

$$R_{\Omega n_L} = \mathbf{n}_{\overline{\Omega}^D} : \mathbf{n}_L \tag{39}$$

in which:

XU ET AL. 17 of 37

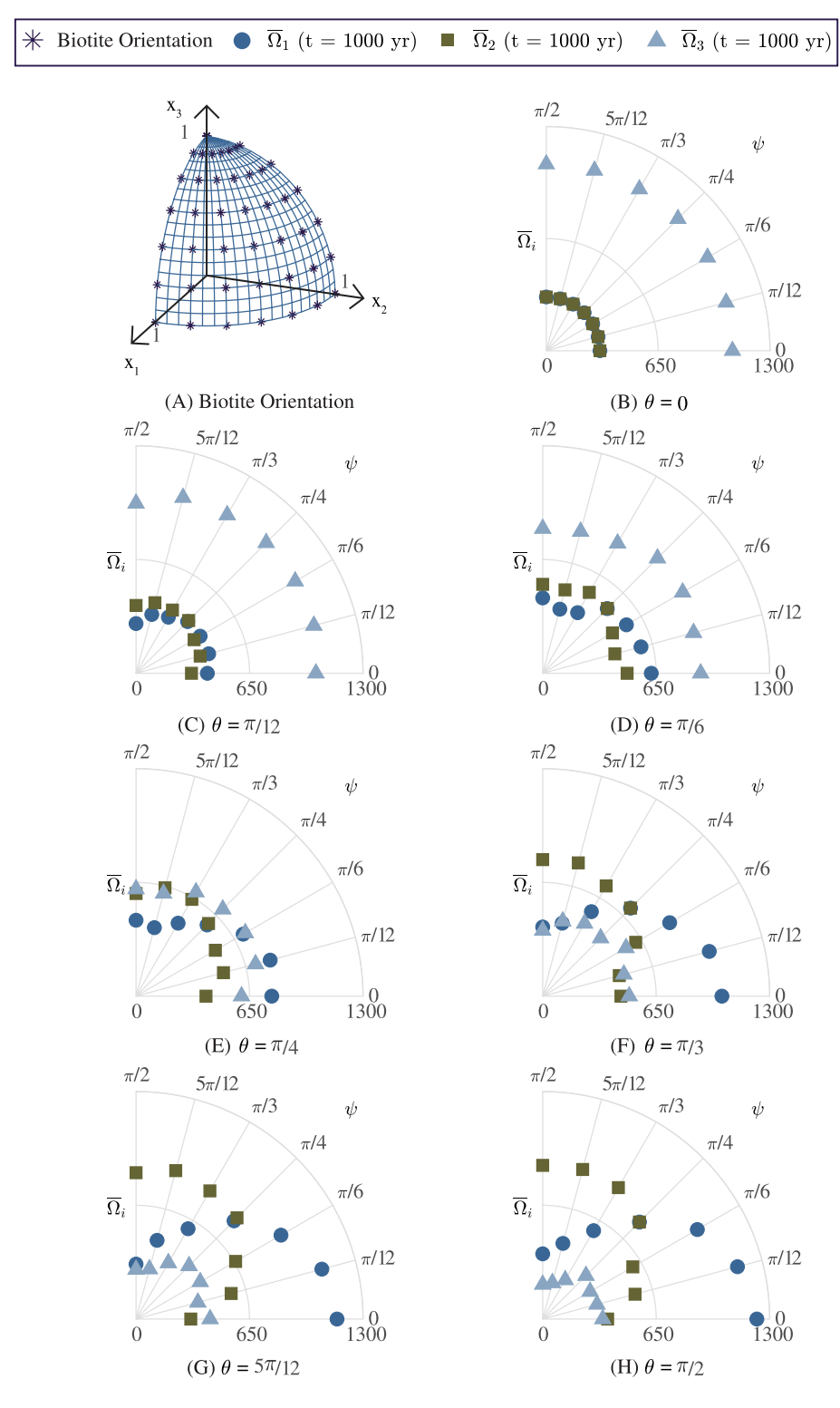


Figure 9. Normalized damage components after 1,000 years of weathering under a proportional loading (K = 0.5; depth = 1,000 m). In (a), each asterisk marks the position of the end of a vector that has its origin at the center of the sphere represented. Each of those vectors represents a biotite expansion direction. By symmetry, only 1/8 of the unit sphere is represented. In (b-h), the circles, squares and triangles respectively mark the values of $\overline{\Omega}_1$, $\overline{\Omega}_2$ and $\overline{\Omega}_3$, which are represented by the radial coordinates. When $\theta = 0$ (Panel b), the damage is transverse isotropic: $\overline{\Omega}_1 = \overline{\Omega}_2$. The damage components vary as function of biotite orientation (angles θ and ψ), indicating that the model can capture the anisotropy of damage.

XU ET AL. 18 of 37



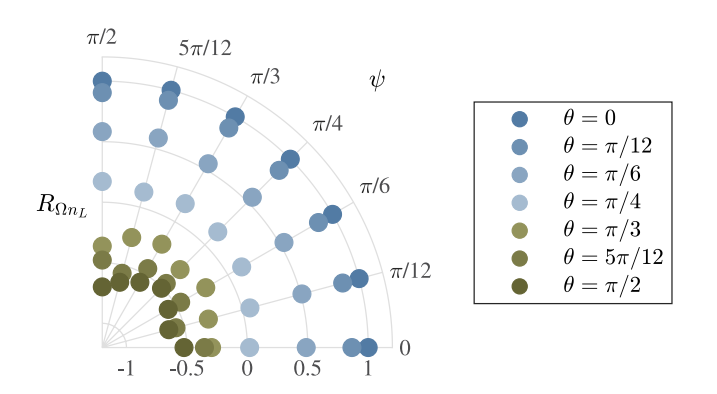


Figure 10. Variation of $R_{\Omega n_L}$ with biotite orientation: relative orientation of damage and loading directions after 1,000 years of weathering under a proportional loading path (K = 0.5; depth = 30 m). $R_{\Omega n_L} = 1$ whenever biotite inclusions are oriented horizontally, that is, when damage and loading directions coincide. The smaller $R_{\Omega n_L}$, the more anisotropy at REV scale.

$$n_{\overline{\Omega}^{D}} = \frac{\overline{\Omega} - \frac{1}{3} \text{tr}\left(\overline{\Omega}\right) I}{\sqrt{\left(\overline{\Omega} - \frac{1}{3} \text{tr}\left(\overline{\Omega}\right) I\right) : \left(\overline{\Omega} - \frac{1}{3} \text{tr}\left(\overline{\Omega}\right) I\right)}}$$
(40)

$$n_L = \frac{\Sigma - \frac{1}{3} \operatorname{tr}(\Sigma) I}{\sqrt{\left(\Sigma - \frac{1}{3} \operatorname{tr}(\Sigma) I\right) : \left(\Sigma - \frac{1}{3} \operatorname{tr}(\Sigma) I\right)}}$$
(41)

are the unit-norm deviatoric directions of damage and loading, respectively. Figure 10 shows the variation of $R_{\Omega n_L}$ with the angles θ and ψ .

By construction, the damage direction coincides with the loading direction when $R_{\Omega n_L}=1$. In Figure 10, we verify that $R_{\Omega n_L}=1$ whenever the biotite grains are oriented horizontally (i.e., at $\theta=0$). The smaller $R_{\Omega n_L}$, the more anisotropy at REV scale. From Figures 9 and 10, we note that for all values of the Euler angle ψ defined in Figure 4, the vertical damage component Ω_3 , which represents the density of crack planes projected along the horizontal axes, decreases with θ , while the horizontal damage components Ω_1 and Ω_2 increase with θ . This can be explained as follows. When biotite inclusions are

horizontal, weathering causes biotite expansion that produces stresses that counteract the overburden stress σ_v imposed on the REV. As biotite orientation grows closer to vertical (i.e., as θ approaches $\pi/2$), biotite expansion induces stresses that counteract the horizontal stress $0.5~\sigma_v$ imposed on the REV. This produces cracks that are oriented progressively closer to vertical, and thus induces progressively more horizontal damage and less vertical damage with increasing θ . This in turn results in a damage direction $\mathbf{n}_{\overline{\Omega}}^{D}$ that deviates progressively more from the loading direction \mathbf{n}_L with increasing θ . This results in the decrease of $\mathbf{R}_{\Omega n_L}$ with θ .

Lastly, the results of this sensitivity analysis indicate that the model proposed in the present study captures the development of non axis-symmetric damage. The difference between the two lateral components of damage is the strongest for $(\psi = 0, \theta \ge \pi/4)$, $(\psi = \pi/2, \theta \ge \pi/4)$ and $(\psi = \pi/6, \theta = \pi/2)$. Although it is difficult to disentangle the effects of biotite expansion versus regional stresses, the results do show that micro-crack orientations are the signature of regional stresses in a bedrock that contains aligned biotite minerals.

By contrast with the model proposed in Shen et al. (2019), the two-step homogenization scheme proposed here highlights how, under the same loading conditions, different biotite orientations can result if different orientations of micro-cracks. This is an essential feature to infer the variation of regional stresses and understand the processes that result in the formation of crack patterns. Given the apparently ubiquitous presence of anisotropy in bedrock due to fabric formation (e.g., as detected by anisotropy of magnetic susceptibility [AMS] measurements (Bouchez, 1997)), the possibility to predict the evolution of cracks in different directions under the influence of weathering is particularly significant.

5. Effects of Biotite Orientation and Weathering Rate Patterns on Damage and Stress in Static Topography

5.1. Implementation of the Model in a Finite Element Scheme

We implemented the model in the FE software ABAQUS in a UMAT subroutine. The FEM allows solving boundary value problems by calculating the displacement in subdomains (the FEs) delimited by nodes and discretized by integration points, which are used to interpolate the deformation and stress fields. The mechanical behavior represented at the integration point is similar to that described in Section 4 at the material point.

In the following, we apply stress boundary conditions at the lateral boundaries of a domain that contains a large number of elements and integration/material points, instead of applying regional stresses at the material point directly. By so doing, we explore the coupled effects of biotite orientation, topography, weathering gradients and erosion on the anisotropy of stress and damage.

XU ET AL. 19 of 37



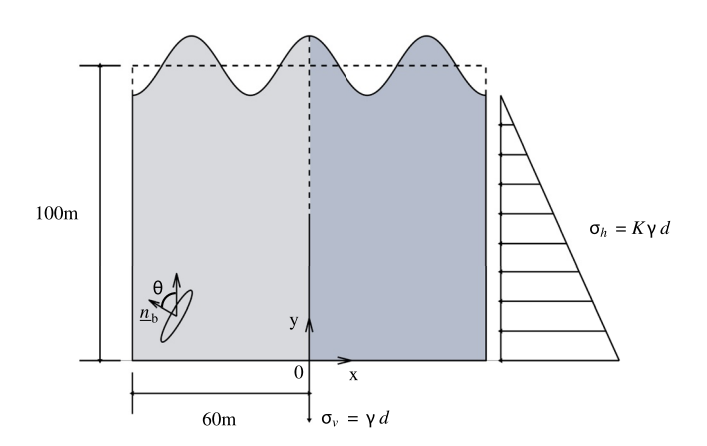


Figure 11. Finite element method simulation set-up to study the influence of biotite orientation on stress and damage distributions upon weathering in lithostatic conditions. The imposed lateral stress boundary condition σ_h increases linearly with depth d. Note: the vector normal to the biotite inclusion in 2D (noted \underline{n}_b) is equivalent to \underline{e}_3' in 3D. The dashed line represents an axis of symmetry of the problem.

The problems that we are interested in here are time-dependent. Boundary conditions are constant, and weathering evolves over time, incrementally changing the state of stress in each element of the domain. The load increment is thus controlled by time. Once the problem has been solved at time t, the solution for the next time increment is found by applying a Newton-Raphson method, which requires calculating the tangent stiffness matrix $\mathbb{C}^{tg} = \partial \Delta \Sigma / \partial \Delta E$ for each material point. The tangent stiffness \mathbb{C}^{tg} is used to compute an initial guess for the nodal displacements at $t + \Delta t$. The corresponding strain increments $\Delta E^{\rm FE}$, together with the stress Σ^t and the set of internal state variables β_i^t corresponding to the previous increment, are used inside the UMAT subroutine to calculate a new state of stress and the corresponding new tangent stiffness. When the state of stress found by the FEM converges to the state of equilibrium, the new values of the stresses, internal variables, and tangent stiffness at $t + \Delta t$ have been found, and the calculation advances to the next increment. The calculation of \mathbb{C}^{tg} is explained in detail in Appendix D.

All the simulations presented in the following are in two dimensions, and we assume plane strain. In practice, this means that the only variable biotite orientation angle is θ (see Figure 11).

5.2. Initial Conditions in Simulations Under Static Topography

To demonstrate the combined effects of topography and biotite weathering on rock damage and strain, we conducted two simulations with the FE implementation of the model. Each simulation considers 1,000 years of biotite weathering in a rock mass under sinusoidal topography (Figure 11). The sinusoidal topography has a mean elevation of 100 m above a reference elevation, described by $y_{top} = 10\cos(\pi x/20) + 100$.

To represent a realistic topography, the FE domain is 60 m wide, and we apply a symmetric boundary condition on the left-hand side (zero horizontal displacement, zero shear stress), so that it is possible to predict the displacement, stress and damage fields over a width of 120 m. The vertical displacement is fixed to zero at the bottom (y = 0); the topographic surface is free of stress; the right-hand-side boundary is subjected to a horizontal stress equal to half the vertical lithostatic stress: $\sigma_h(d) = 0.5 \gamma d$, with d for depth, counted from the free surface of the domain $(d = y_{\text{top}} - y)$, and γ for the rock specific weight. The constitutive parameters used to represent the bedrock rock are summarized in Table 1.

In each simulation, we apply a biotite weathering rate that decreases with depth, such that the bedrock experiences faster weathering closer to the surface than at depth. In the first simulation, the biotite weathering rate pattern is out of phase with the topography (Figure 13a): the biotite weathering rate decreases with depth following sinusoidal curves that are shifted by a phase of $\pi/2$ relative to the sinusoidal topography ($y_{\text{sim},1} = -10\cos(\pi x/20) + 70$), indicating that the decreasing gradient of biotite weathering rate is the steepest under the valleys and the smoothest under the hills. In the second simulation, we apply a surface-parallel weathering pattern in phase with the topography ($y_{\text{sim},2} = 10\cos(\pi x/20) + 70$), in which the weathering rate decreases linearly with depth from the surface down to a depth of 30 m below the surface (Figure 14a). These biotite weathering rate patterns are chosen to mimic end-member patterns of bedrock fracture density modeled in St. Clair et al. (2015).

The two simulations considered here differ only in the spatial pattern of biotite weathering rate, which only affects stress distributions for t > 0, since at time zero, a lithostatic state of stress is applied to the rock mass $(\sigma_v(d) = \gamma d)$ in the whole domain, and $\sigma_h(d) = 0.5 \gamma d$ at the lateral boundaries).

After each simulation is initiated, the biotite weathering rate decreases over time at all depths as $R(y, t) = \alpha(y)10^{-12.32}t^{-0.603}$, where $10^{-12.32}t^{-0.603}$ is that of Equation 36 and represents the decay of the weathering rate over time (White & Brantley, 2003). The function $\alpha(y)$ is introduced to represent a decrease of biotite weathering rate with vertical distance below the free surface. We set $\alpha(y = y_{top}) = 1$ to indicate that the weathering rate is the highest at the free surface and we set $\alpha(y = y_{sim,j}) = 0$ to indicate that the weathering rate goes to zero at the bottom of the weathering region. Here j = 1 for the simulation in which the biotite weathering rate is out of phase

XU ET AL. 20 of 37



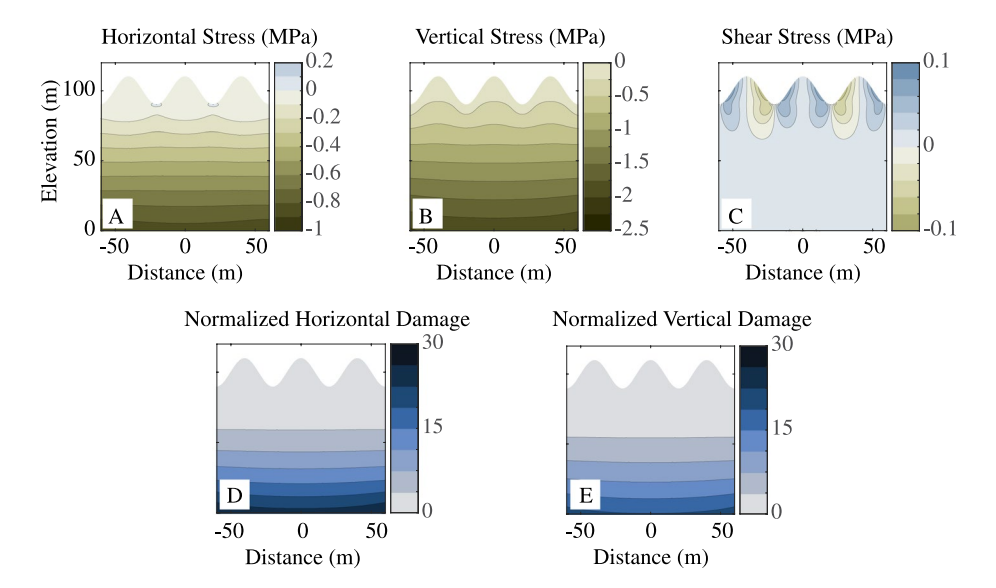


Figure 12. Pre-weathering state (at t = 0). Distributions of stress components (in MPa): horizontal stress (a), vertical stress (b), shear stress (c). Normalized damage component in horizontal (d) and vertical (e) directions.

with the topography, and j=2 for the simulation in which the biotite weathering rate is in phase with the topography. In the simulations presented here, we opt for a linear variation as $\alpha(y) = (y - y_{\text{sim},j})/(y_{\text{top}} - y_{\text{sim},j})$ to indicate that the weathering rate progressively decreases between y_{top} and $y_{\text{sim},j}$ (j=1 for out-of-phase weathering rate, j=2 for in-phase weathering rate). This is intended to mimic a decrease in the intensity of factors driving biotite weathering rate with depth, such as might occur through a progressive decrease in dissolved oxygen with depth.

Figure 12 shows the distribution of stresses and damage before weathering (at t = 0). The vertical stress (σ_{yy}) follows the gravity gradients. The topography has a negligible influence on the vertical stress at depth due to the small height of the hills compared to the depth considered (10%), that is, the absence of rock mass in the valleys does not translate into significantly less vertical stress at depth. Since the model is in plane strain, horizontal stresses exist in-plane and out-of-plane. Both the in-plane and out-of-plane horizontal stresses follow the lithostatic gradient (only σ_{xx} is shown). They are of same order of magnitude, that is, half of the vertical stress at same depth. Of note, a slight horizontal tension is noted in the valleys, due to the unconstrained horizontal extension of the free surface (where the in-plane horizontal stress applied at the boundaries is zero). The shear stress is zero except close to the free surface, and represent the resistance of the bedrock to the sliding that would occur along the slope of the hills under the influence of gravity without horizontal confinement (which acts at the foot of the hills and lower).

Before weathering occurs, damage accumulation is driven by the macroscopic deformation energy. The relative damage components are zero at depths of 50 m or less. At depth, the vertical compression stress is twice higher than the horizontal compression stress. As a result, vertical cracks tend to open, which explains why at depths greater than 50 m, the horizontal damage component follows the gradient of gravity. Although of lower magnitude, the vertical damage component follows the same trend. This can be explained by the horizontal compression stresses that act both in-plane and out-of-plane in plane strain conditions.

Figures 13 and 14 show the distributions of stress and damage after 1,000 years of weathering with the two weathering rate distributions shown in Figures 13a and 14a, for five biotite orientations: $\theta = 0$, $\pi/6$, $\pi/4$, $\pi/3$, $\pi/2$. The results are discussed in the two following subsections.

5.3. Stress Responses

5.3.1. Horizontal Stress

Biotite weathering reverses the sign of the horizontal stress in the valleys, which switches from tension to compression (Figures 13b1–13b5 and 14b1–14b5). When biotite minerals are vertical or inclined, biotite expansion is

XU ET AL. 21 of 37

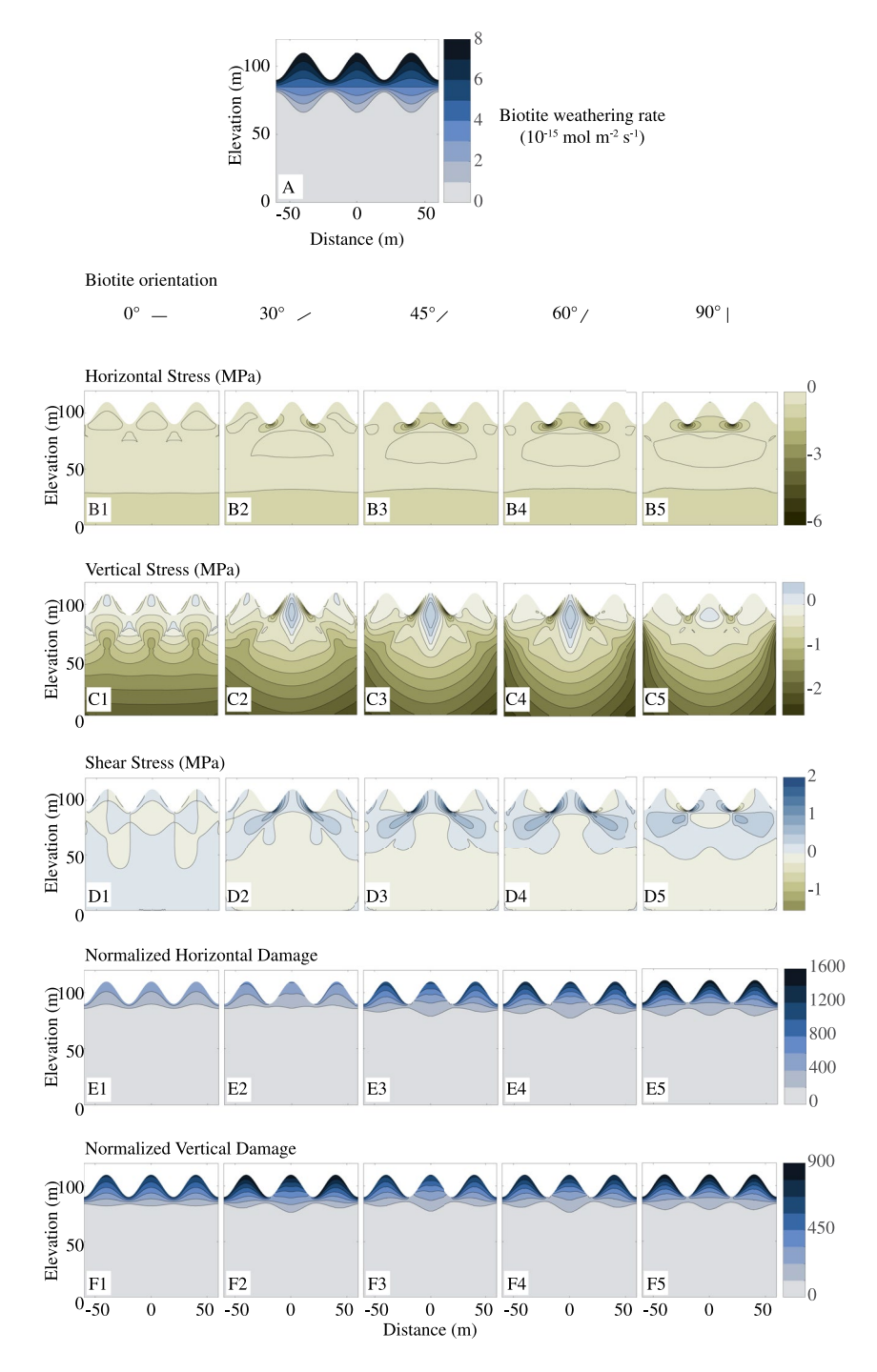


Figure 13. Distributions of stress (in MPa) and normalized damage for different biotite orientations with weathering gradient distribution out of phase with topography.

constrained by the horizontal stress applied at the lateral boundaries of the domain, which produces this horizontal compression. When biotite minerals are horizontal or close to horizontal, biotite expansion gets closer to the vertical. A slight horizontal compression is generated in the valleys because of Poisson's effects: biotite minerals shrink slightly in their longitudinal direction, and that shrinkage, mostly in the horizontal direction, is not restricted by the boundary conditions. At larger depths, biotite weathering has little effect on the horizontal stress, which remains similar to the initial stress due to the field gravity. This is due to the fact that weathering is only active in the first 30 m down from the free surface.

XU ET AL. 22 of 37

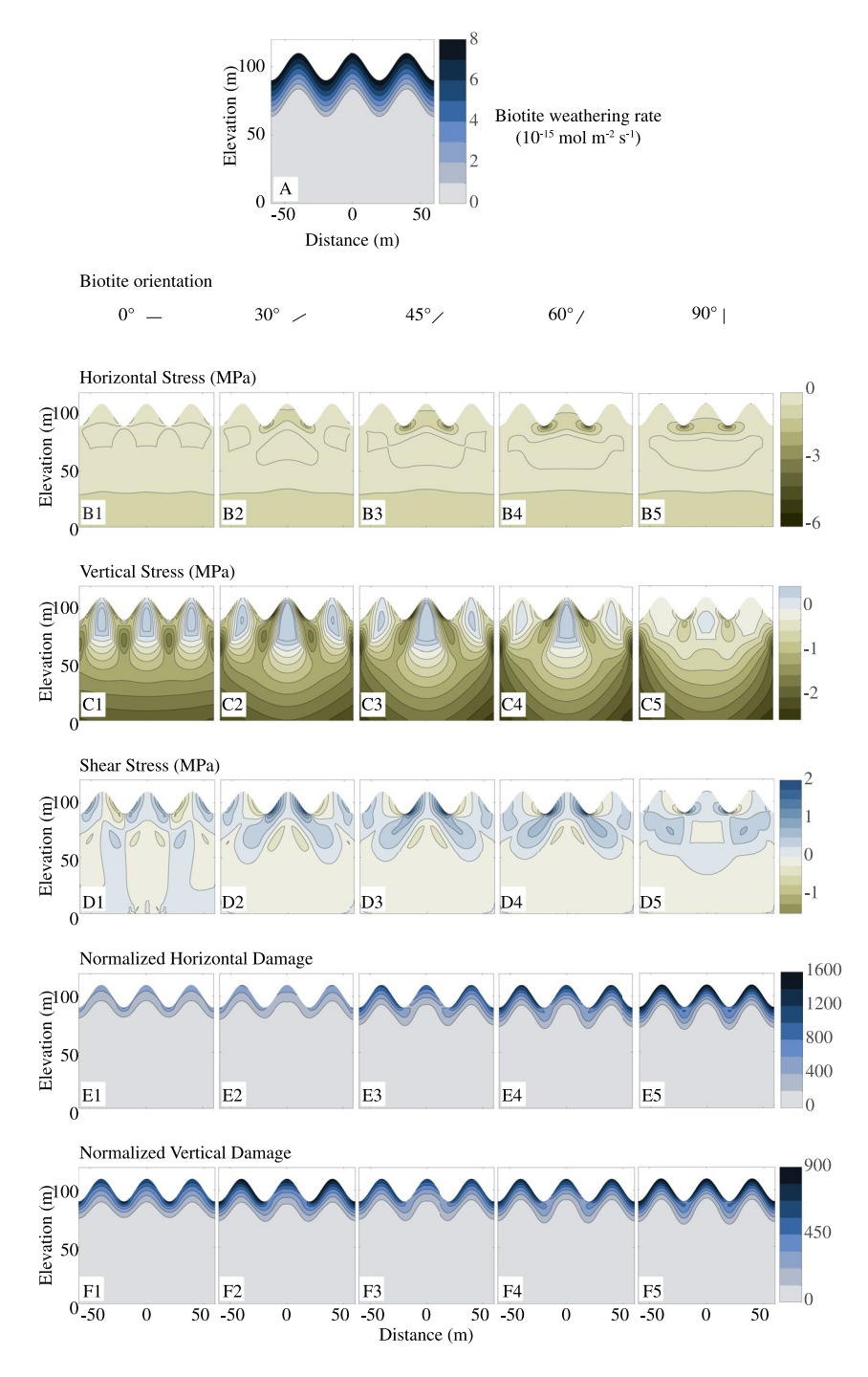


Figure 14. Distributions of stress (in MPa) and normalized damage for different biotite orientations with weathering gradient distribution in phase with topography.

5.3.2. Vertical Stress ($\theta < \pi/2$)

Biotite expansion in the vertical direction horizontal or inclined biotite minerals is not constrained by any overburden stress and induces vertical tensile stress in the hills for all cases under study (Figures 13c1-13c5 and 14c1-14c5). When biotite minerals are inclined ($\theta = \pi/6$, $\theta = \pi/4$ and $\theta = \pi/3$) and the weathering gradient is out of phase with the topography, differential heave between the bedrock within and below the hills and the bedrock under the valleys results in larger vertical tensile stress in the central hill than in the lateral ones. Under

XU ET AL. 23 of 37



the same weathering gradient, when the biotite minerals are horizontal (Figure 13c1), the bedrock at the top of the hills and at shallow depth under the valley are subjected to vertical tensile stress. The vertical stress becomes compressive 20 m below the free surface both in the hills and under the valleys because of the differential heave of points that are at same depth but under a hill versus under a valley. When the weathering gradient is out of phase (respectively, in phase) with the topography, the weathering rate is lower (respectively, higher) at a given depth under the valleys than it is under the hills. As a result, a stress develops to counteract the relative displacement of the bedrock that would otherwise occur under the sole effect of weathering under the hills. This explains why compression stress accumulates under the valleys for the in-phase topography (in reaction to the slower relative vertical displacement of the hills), while there is a slight vertical tensile stress in the valleys of the out-of-phase topographies.

5.3.3. Vertical Stress ($\theta = \pi/2$)

When $\theta = \pi/2$, the distribution of vertical stress is similar for both weathering gradient distributions (Figures 13c5 and 14C5). When biotite minerals are vertical, weathering-induced expansion is horizontal, and yet, vertical compression concentrates in the valleys and vertical tension is observed in the central hill. In that case, the horizontal biotite expansion in the lateral hills occurs free of horizontal stress, which puts the central hill under horizontal compression (according to the principle of mechanical action/reaction). In the absence of vertical overburden stress, the bedrock in the central hill is subjected to a vertical expansion by Poisson's effects, which translates into vertical tensile stress. These Poisson's effects disturb the pre-weathering state of stress at larger depth than when the biotite minerals are horizontal or inclined. In general, weathering lowers the compression stress that would occur under the sole effect of gravity, the larger effects being noted at the center of the domain, due to the boundary conditions adopted in this problem.

5.3.4. Shear Stress ($\theta < \pi/2$)

Shear is undisturbed beyond 50 m in depth below the valleys. Two points in the weathering zone that have the same depth but a different position along the horizontal direction are likely to be subjected to different weathering rates, which induces differential heave and shear stress, especially for the weathering rate gradient that is in phase with the topography. For both weathering rate distributions, shear bands inclined at 45° develop at the feet of the central hill when the biotite minerals are inclined ($\theta = \pi/6$, $\theta = \pi/4$, and $\theta = \pi/3$), because the weathering induced stresses (tension in the expansion direction, and compression in the orthogonal direction due to Poisson's effects) are the most constrained in the central hill, which is restrained by the two lateral hills. Of note, when the biotite minerals are horizontal, almost no shear stress develops when the weathering rate distribution is out-of-phase with the topography (in contrast with the in-phase topography). This is because two neighboring points at same, shallow depth undergo similar expansion, and because that expansion is constrained by almost no overburden stress. This leads to a quasi-zero differential heave.

5.3.5. Shear Stress ($\theta = \pi/2$)

The shear stress distribution is similar for both weathering gradient distributions when biotite minerals are vertical (Figures 13d5 and 14d5), indicating high shear stress concentrations at the feet of the central hill, and a no-shear stress region under the central hill. Since in that case, biotite expansion occurs horizontally, weathering does not induce differential heave except by Poisson's effects, and the effect of weathering on shear stress is similar for both weathering distributions.

5.4. Damage Responses

Our initial hypothesis was that the distribution of damage was the result of two concurrent phenomena: the expansion of biotite minerals over time, which occurs faster close to the topographic surface in our simulations, and the increase of regional compression stresses with depth, in a pattern that depends on the imposed stress boundary conditions and the overlying topography. There exists indeed a vertical gradient of damage starting at a depth of 50 m before weathering occurs (Figure 12). However, the magnitude of the normalized damage components is of the order of 30 at most (which means that the application of the lithostatic stress gradient multiplied the reference crack densities Ω^0_{xx} and Ω^0_{yy} by 30). The simulations show that the maximum damage in the bedrock is

XU ET AL. 24 of 37



10–60 times more intense after 1,000 years of weathering than it was before weathering. In other words, damage is almost entirely associated with biotite expansion, not the lithostatic stress conditions.

The distribution of damage follows the gradient of weathering rate regardless of topography in Figures 13e1–13f5 and 14e1–14f5, with more intense damage toward the top, where the weathering rate is highest. This observation is in agreement with Figure 8, which shows that the energy release necessary to propagate cracks (Equation 27) is dominated by the biotite inclusion eigenstress, should the cracks be parallel or orthogonal to the biotite inclusions. Our results thus suggest that the weathering gradient is the main controlling factor of the spatial distribution of damage for the regional stresses simulated.

Damage accumulated during the 1,000 years of weathering is located in the zone subject to weathering, not beyond. The horizontal damage component $(\overline{\Omega}_{xx})$, which represents the volume fraction of vertical crack planes, is smaller than the vertical damage component $(\overline{\Omega}_{yy})$ when $\theta = 0$ and $\theta = \pi/6$, while $\overline{\Omega}_{xx} > \overline{\Omega}_{yy}$ when $\theta = \pi/3$ and $\theta = \pi/2$. Both components reach similar values at similar depths when $\theta = \pi/4$. These observations are consistent with the result shown in Figure 8, which indicates that more energy is released toward the propagation of cracks that are aligned with the biotite inclusions (i.e., cracks that open in the direction of biotite expansion). Additionally, the damaged zone is larger for greater values of θ (i.e., when biotite inclusions are more vertical). When biotite minerals are close to vertical, tensile horizontal stress concentrates in the valleys (Figures 13b4–13b5 and 14b4–14b5). This means that deformation energy is stored instead of being released in the form of damage. This explains why less horizontal damage occurs in the valleys in these cases (Figures 13e4–13e5 and 14e4–14e5).

6. Effects of Biotite Orientation and Weathering Rate Patterns on Damage and Stress in Eroding Topography

6.1. Principle of the Finite Element Model of Erosion With Weathering

To explore the effects of erosion on damage and stress, we now conduct simulations identical to those in Section 5 for biotite inclusions oriented at $\theta = \pi/2$, except that here the topographic surface erodes downward instead of remaining static. Elements that are the top of the FEM model are removed according to a linear function of time, at a rate of $\Delta y = \lambda t$ with $\lambda = -20$ m/Myr (to simulate mass removal by erosion). At all times in the simulations, the biotite weathering rate pattern migrates downward with the topographic surface, such that the biotite weathering rate is always the highest at the topographic surface and declines with depth: $R(y, t) = \alpha(y, t)10^{-12.32}t^{-0.603}$.

The free surface and the lower boundary of the weathering zone at time zero are set as the same functions as in Section 5: $y_{\text{top}}^{t=0} = 10\cos(\pi x/20) + 100$, $y_{\text{sim},1}^{t=0} = -10\cos(\pi x/20) + 70$, $y_{\text{sim},2}^{t=0} = 10\cos(\pi x/20) + 70$. The top and bottom surfaces of the weathering zone move at the same speed: $y_{\text{top}} = y_{\text{top}}^{t=0} + \lambda t$; $y_{\text{sim},1} = y_{\text{sim},1}^{t=0} + \lambda t$; $y_{\text{sim},2} = y_{\text{sim},2}^{t=0} + \lambda t$. Like in Section 5, $\alpha(y,t)$ takes the value 1 at the free surface (maximum weathering rate) and the value 0 at the lower boundary of the weathering zone (no weathering), and is interpolated linearly with depth between these two values to mimic a progressive decay of biotite weathering rate with depth. We opt for a linear variation as $\alpha(y,t) = (y-y_{\text{sim},j})/(y_{\text{top}}-y_{\text{sim},j})$, with j=1 (out-of-phase weathering rate) or j=2 (in-phase weathering rate). The elevation of the upper boundary of the weathering surface changes with erosion, but the value of $\alpha(y,t)$ at the free surface is one at all times.

Figures 15 and 16 show the evolution of stress and damage driven by biotite weathering gradients out-of-phase and in-phase with the eroding topography, respectively. The altitude of the top of the hills decreases by 10 m over the 500-kyr duration of the simulations through the imposed erosion function. The imposed biotite weathering rate decreases over time (Figures 15a1–15a5 and 16a1–16a5) under the same relation applied in the static-topography simulations.

6.2. Stress Responses

The stress distributions in the eroding-topography simulations share many characteristics with those in the static-topography simulations (compare Figures 13b5, 13c5, 13d5 and 14b5, 14c5, 14d5 to Figures 15b5, 15c5, 15d5 and 16b5, 16c5, 16d5). Most striking are the concentration of horizontal tensile stress in the valleys, development of tensile vertical stress in the hills, shear bands at the feet of the hills, and a zone of zero-shear stress below the central hill. The spatial patterns of shear stress are similar to those in the static-topography simulations,

XU ET AL. 25 of 37

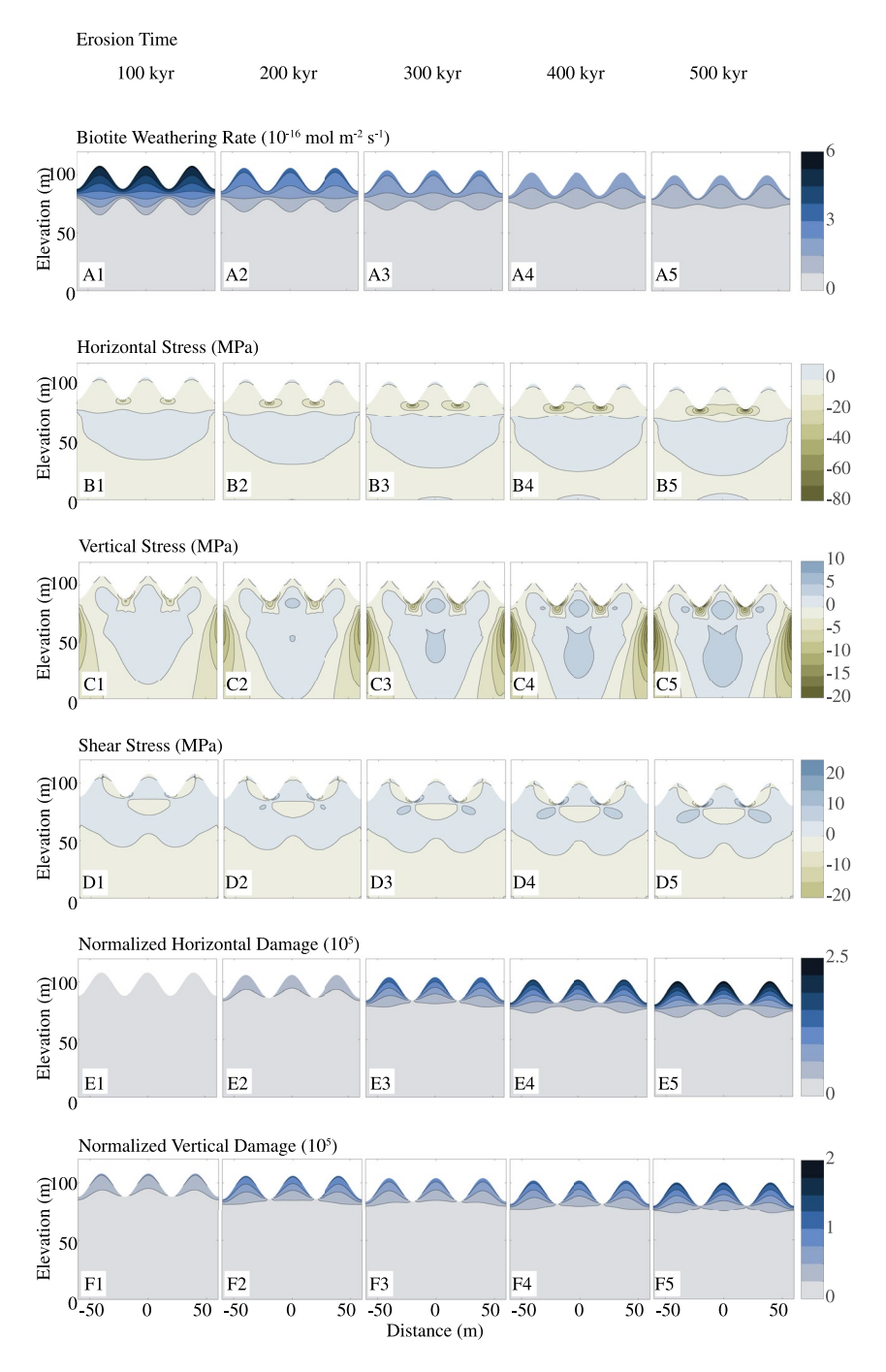


Figure 15. Distributions of weathering gradient out of phase with the topography combined with erosion. Resulting stress components (in MPa) and normalized damage components for different biotite orientations.

but the magnitude grows larger over time (Figures 15d1–15d5 and 16d1–16d5). This is because biotite weathering is simulated over a longer period of time, which results in more horizontal biotite expansion and thus more horizontal tensile stress in the bedrock.

Interestingly, over a period of 100 kyr or more, a zone of tensile horizontal stresses develops under the hills down to a depth of about 50 m (Figures 15b1–15b5 and 16b1–16b5). While the tensile vertical stress was concentrated in the hills after 1,000 years of weathering without erosion, the tensile vertical stress extends to almost the entire domain under study after 100,000 years of weathering with erosion, and stays about the same even after

XU ET AL. 26 of 37

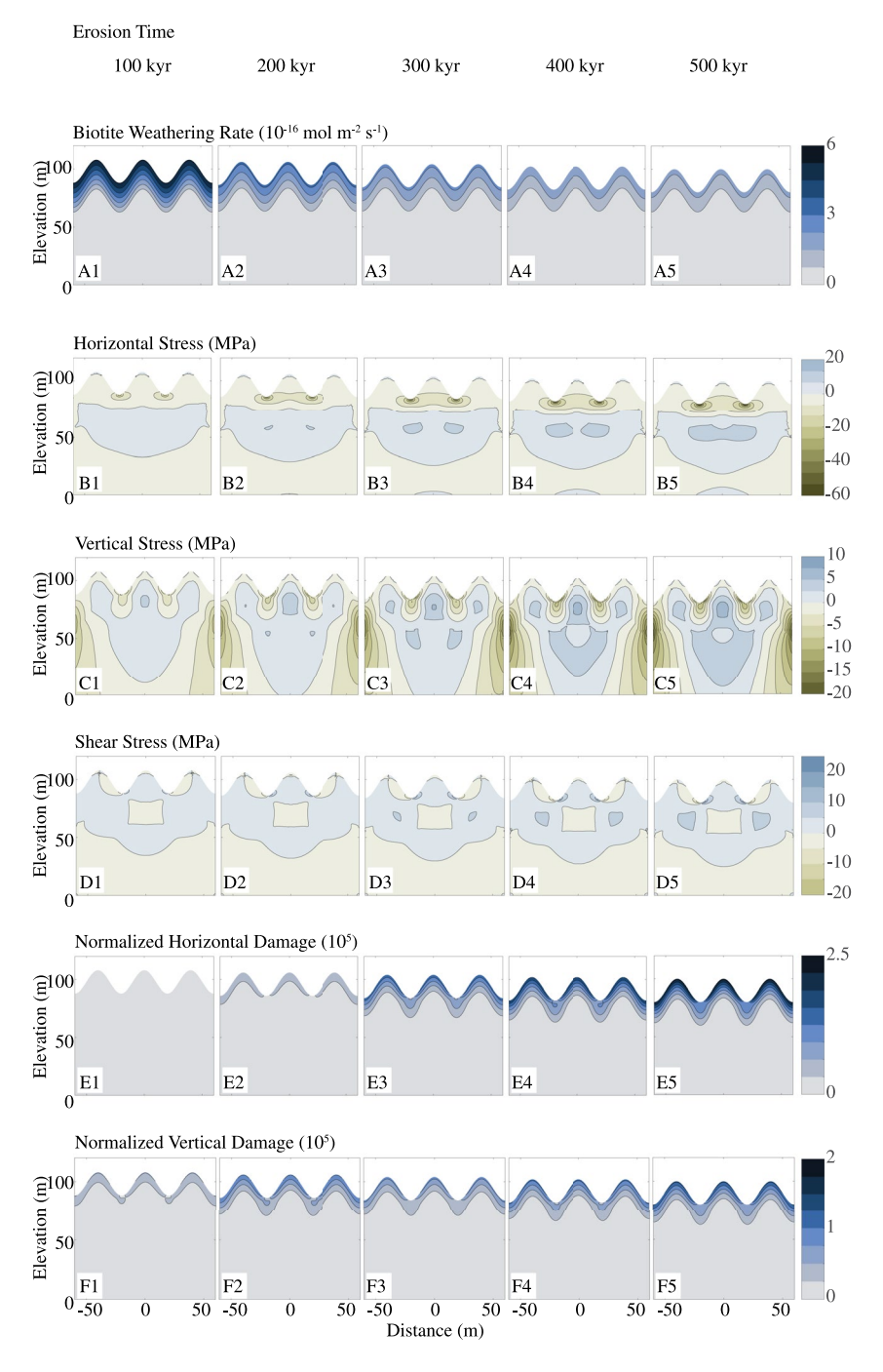


Figure 16. Distributions of weathering gradient in phase with the topography combined with erosion. Resulting stress components (in MPa) and normalized damage components for different biotite orientations.

500,000 years (Figures 15c1–15c5 and 16c1–16c5). Moon et al. (2017, 2020) observed weathering-induced rock damage as deep as 500 m. Our FEM model cannot capture weathering-induced micro-crack propagation at that depth because it does not account for the growth of the weathering zone with fluid transport through micro-cracks. The acceleration of the weathering rate with exposure to fluids flowing through cracks could be simulated in future work. Despite its purely mechanical nature, the proposed model captures the wide influence of weathering on the stress field, which extends far beyond the weathering zone (more than 50 m away under the present boundary conditions). The development of large zones of tensile stress can be explained by two phenomena.

XU ET AL. 27 of 37



6.2.1. More Biotite Lateral Expansion Leads to More Tensile Stress Build-Up in the Direction Orthogonal to Mineral Expansion

Inclined and horizontal (respectively, vertical) biotite minerals are subjected to vertical expansion (respectively, horizontal expansion). The matrix around the inclusions is thus subjected to a vertical (respectively, horizontal) tensile stress field if it is free to expand vertically (respectively, horizontally), and to a vertical (respectively, horizontal) compression stress field otherwise. The extension of the zone of tensile stress between 1,000 years of weathering (Figures 15b1–15c5 and 16b1–16c5) and 100 kyrs or more (Figures 15b1–15c5 and 16b1–16c5) seems to indicate that over time, the expansion of the weathering minerals overcomes the compression constraint imposed by the lithostatic stress field in a large part of the bedrock under the hills.

6.2.2. Poisson's Effects at Inclusion Scale Overcomes the Deformation of the Matrix Due To the Lithostatic Stress Field

Inclined and vertical (respectively, horizontal) biotite minerals are subjected to horizontal expansion (respectively, vertical expansion) because of the weathering eigenstress, and are subjected to vertical shrinkage (respectively, horizontal shrinkage) by Poisson's effects. The biotite inclusions and the matrix around them shrink vertically because of the field of gravity and horizontally, because of the applied lateral boundary conditions. But the shrinkage due to the lithostatic stress field is less than the vertical (respectively, horizontal) compression deformation undergone by the biotite inclusions due to weathering. The vertical shrinkage (respectively, horizontal shrinkage) due to weathering is restricted by the bedrock matrix. The resulting differential deformation between the biotite inclusions and the matrix results in the production of a tensile stress in the matrix around the biotite inclusions, which translates into a net tensile vertical stress (respectively, net horizontal stress) in the bedrock.

6.3. Damage Responses

As in the static-topography simulations, the spatial distribution of damage in the eroding-topography simulations (Figures 15e1–15f5 and 16e1–16f5) follows the imposed pattern of biotite weathering rate, with more intense damage close to the topographic surface and no damage deeper than the zone subject to biotite weathering. As described in Section 5, this is because the energy release necessary to trigger damage propagation is mostly contributed by the weathering eigenstress of the biotite minerals. At a given depth and time, the horizontal damage is about two times larger than the vertical damage. This is because cracks mostly propagate in planes parallel to the biotite inclusions, which are vertical in this simulation and hence produce mostly horizontal damage (i.e., crack planes with horizontal normals).

Despite the continuous removal of the most damaged rock layers by surface erosion, the intensity of damage at the freshly exposed free surface increases over time. This means that in the problem under study, the accumulation of damage is dominated by the biotite weathering rate and not the erosion rate. In simple terms, erosion does not occur fast enough to remove rock layers before they get damaged by weathering. There is enough time between two iterations of erosion to accumulate damage in the bedrock.

7. Implications for Biotite's Role in Critical Zone Evolution

Figures 13–16 show that spatial patterns in damage closely follow the imposed patterns in biotite weathering rate in both the eroding and non-eroding simulations. By contrast, they differ strongly from the spatial patterns in the initial stress field (Figure 12), which were imparted by the stress boundary conditions and the topography before biotite weathering began. This implies that the dominant driver of damage in these simulations is biotite weathering. Even if the simulations were conducted for specific boundary conditions, it is interesting to note that, under common conditions, weathering can dominate the effects of tectonic and topographic stresses in the propagation of damage in the bedrock.

The ability of biotite to damage bedrock in these simulations is consistent with longstanding hypotheses that propose a central role for biotite in regolith production and landscape evolution. For example, Wahrhaftig (1965) posited that biotite expansion was the primary driver of rock disintegration in the granitic southern Sierra Nevada, and that geographic variations in biotite weathering could have helped generate the region's characteristic stepped topography (Callahan et al., 2019). Likewise, this is consistent with the hypothesis that mineral expansion during

XU ET AL. 28 of 37



weathering controls the production of spheroidal fractures during corestone development (Fletcher et al., 2006) and the production of weathered saprolite (Buss et al., 2008, 2013; Goodfellow et al., 2016).

Figures 13–16 are useful because they reveal the magnitude of biotite-generated damage relative to those generated by topographic and tectonic stresses. On their own, these simulations cannot quantify the relative magnitude of these sources of damage in all landscapes, because these simulations were conducted under a narrow range of lithologic, topographic, and tectonic conditions. In nature, each of these factors varies geographically and in time. The degree to which topographic stresses damage rock depends on the amplitude and wavelength of the topography (Miller & Dunne, 1996; Molnar, 2004; Moon et al., 2020; Slim et al., 2015; St. Clair et al., 2015), and the degree to which tectonic forces promote or inhibit damage depends on the strength and direction of those forces. Both of these factors vary substantially in space. Thus, in any given landscape, the patterns and magnitudes of damage depend on the shape and scale of the topography, the magnitude and orientation of the tectonic stresses, and the abundance and orientation of the biotite inclusions. Despite the spatial variability of regional stresses and mineralogy, our results show that biotite orientation could, to some extent, change the relation between regional stresses and the shape of the Critical Zone/bedrock interface as highlighted in St. Clair et al. (2015), and lead to a more surface-parallel Critical Zone architecture. In metamorphic rocks like schists and gneisses with strong expression of preferential biotite orientation, variations in critical zone thickness could be explained by variations in damage caused by the orientation of biotite relative to regional stress.

Determining the conditions that govern the relative importance of biotite weathering in damage production will require exploring the sensitivity of rock damage to a wide range of topographies, regional stress fields, and biotite characteristics. This is beyond the scope of this study, but the model developed in Sections 2 and 3 is well suited for this task in future work. A unique feature of this model is that it computes the stresses and damage fields generated by mineral weathering as well as those generated topographic and regional stresses. This distinguishes it from models that compute stress fields from topographic and regional forces but do not account for mineral weathering, as well as models that account for mineral weathering but not topographic or regional stresses.

By showing that biotite weathering can dominate damage production, these simulations support the idea that the mineral characteristics can modulate feedbacks between lithology, rock strength, and landscape evolution. For example, Figures 13–16 imply that biotite abundance and orientation should influence saprolite strength. If soil production rates decrease with saprolite strength (e.g., as observed in Heimsath and Whipple 2019), then high biotite abundances should promote faster rock damage, faster soil production, and thicker soils. If downslope soil fluxes increase with soil thickness (Roering, 2008), then landscapes underlain by biotite-rich lithologies should produce higher sediment fluxes and erosion rates, all else equal. Similarly, Figures 13–16 show that biotite weathering can affect shear stress fields in the weathered rock. If these shear stresses patterns are oriented parallel to the hillslope and are sufficiently large, they could affect a hillslope's susceptibility to bedrock landsliding. All of these are consistent with a strong link between lithology and topography.

8. Conclusions

The main contribution of this study is a new model for the development of anisotropic damage and stress in bedrock under the combined influences of biotite weathering, regional stresses, and topographic stresses. To our knowledge, these influences have not been considered simultaneously in a single model before. To demonstrate the behavior predicted by this model, we conducted a series of numerical simulations in bedrock under gently rolling topography, a range of biotite orientations, and two contrasting spatial patterns in biotite weathering rate.

Several behaviors emerge from these simulations. First, the spatial patterns of damage closely follow the imposed pattern in biotite weathering rate, implying that damage can be far more sensitive to biotite weathering than to topographic or regional stresses near Earth's surface (roughly <100 m). According to our simulations, over a 1,000-year duration, biotite weathering produces 10–50 times more crack volume than that generated under topographic and regional stresses alone. The eigenstress associated with biotite weathering dominates the propagation of microcracks over the deformation energy of the bedrock. The same behavior holds in the simulations under slowly eroding topography as under static topography.

Second, the post-weathering stress field differs strongly from the pre-weathering stress field, implying that bedrock stresses are strongly affected by biotite weathering (at least under the boundary conditions used in the simulations).

XU ET AL. 29 of 37



Relative to the stresses imparted by the topographic and regional stresses alone, the stress field after 1,000 years of weathering or more exhibits higher magnitudes, wider shear stress zones at the feet of hills, more tensile vertical stress below the hilltops, and more compressive horizontal stress concentrated in the valleys. Over longer periods of time (500 kyr), horizontal tensile stress develops under the hills and vertical tensile stress develops under and in the hills, likely because of the accumulation of biotite lateral expansion and differential shrinkage between the matrix and the inclusions in the direction orthogonal to biotite expansion (by Poisson's effects). The spatial patterns of stress are largely uncorrelated with the spatial patterns of damage, that is, unlike the damage field, the patterns in the post-weathering stress field are not similar to the pattern of the imposed biotite weathering rate pattern.

Third, the direction of microcracks tends to align with that of the biotite minerals. The behavior of the damaged bedrock is axis-symmetric when the biotite minerals are horizontal (i.e., when the expansion direction aligns with the major principal stress direction). The orientation of the cracks rotates with the orientation of the biotite minerals, becoming more vertical as biotite minerals become more vertical.

Collectively, these observations suggest that mineral weathering can indeed influence fracture dynamics in biotite-bearing rock and that lithology can steer the evolution of Critical Zone architecture. More specifically, the expansion of weathering biotite can propagate fractures in a rock matrix, and biotite orientation can influence the bedrock stress field and the directions of crack growth. This supports the idea that biotite weathering plays a key role in primary porosity development and regolith production, which implies that biotite abundance and orientation should influence a landscape's capacity for water storage and transmissivity. The model developed here presents an improved basis for interpreting observations of biotite and micro-fracture orientation in the field, and thus can help elucidate the influence of mineral weathering on Critical Zone evolution.

Appendix A: Expression of Polarization Tensor

Noting ω and ζ_3 the angular position and the longitudinal coordinate, respectively, we define:

$$\bar{\zeta}_i = \zeta_i / a_i;$$

$$\zeta_1 = \left(1 - \zeta_3^2\right)^{1/2} \cos \omega;$$

$$\zeta_2 = \left(1 - \zeta_3^2\right)^{1/2} \sin \omega;$$

$$\zeta_3 = \zeta_3$$
(A1)

where a_1 , a_2 , and a_3 are the lengths of the semi-axes of the ellipsoidal inclusion, expressed in a rectangular Cartesian coordinate system.

The expression of the polarization tensor depends on the Green's function as follows (Mura, 1987):

$$P_{ijmn} = \frac{1}{8\pi} \int_{-1}^{1} d\zeta_3 \int_{0}^{2\pi} \left(G_{imjn} \left(\bar{\zeta} \right) + G_{jmin} \left(\bar{\zeta} \right) \right) d\omega \tag{A2}$$

where G is the second derivative of Green's function expressed in Fourier space. It is defined as:

$$G_{ijkl}(\bar{\zeta}) = \bar{\zeta}_k \bar{\zeta}_l N_{ij}(\bar{\zeta}) / D(\bar{\zeta})$$
(A3)

in which N_{ii} and D are respectively the cofactor and determinant of a tensor K_{ii} defined as:

$$K_{ik} = C_{ijkl}\bar{\zeta}_j\bar{\zeta}_l \tag{A4}$$

By definition, N_{ii} and D are expressed as:

$$D(\bar{\zeta}) = \epsilon_{mnl} K_{m1} K_{n2} K_{l3}; \tag{A5}$$

$$N_{ij}(\bar{\zeta}) = \frac{1}{2} \epsilon_{ikl} \epsilon_{jmn} K_{km} K_{ln}; \tag{A6}$$

where ϵ_{ijk} is the permutation tensor and C_{ijkl} is the matrix stiffness tensor. When the inclusions are embedded in a general anisotropic matrix, there is no explicit formula to calculate the components P_{ijmn} , so in these cases we apply a numerical method to evaluate the Hill's tensor \mathbb{P}_i (Gavazzi & Lagoudas, 1990).

XU ET AL. 30 of 37



Appendix B: Relation Between the Derivative of a Tensor and the Derivative of Its Inverse

Consider a tensor M, of inverse N, and suppose that both M and N depend on the variables χ and ζ . We have:

$$0 = \frac{\partial \mathbb{I}}{\partial \chi} = \frac{\partial \left(\mathbb{M}(\chi, \zeta) : \mathbb{N}(\chi, \zeta) \right)}{\partial \chi}$$

$$= \frac{\partial \mathbb{M}(\chi, \zeta)}{\partial \chi} : \mathbb{N}(\chi, \zeta) + \mathbb{M}(\chi, \zeta) : \frac{\partial \mathbb{N}(\chi, \zeta)}{\partial \chi}$$
(B1)

So, we get:

$$\frac{\partial \mathbb{M}(\chi, \zeta)}{\partial \chi} = -\mathbb{M}(\chi, \zeta) : \frac{\partial \mathbb{N}(\chi, \zeta)}{\partial \chi} : \mathbb{N}(\chi, \zeta)^{-1}$$
(B2)

From which, we conclude:

$$\frac{\partial \mathbb{M}(\chi,\zeta)}{\partial \chi} = -\mathbb{M}(\chi,\zeta) : \frac{\partial \mathbb{M}(\chi,\zeta)^{-1}}{\partial \chi} : \mathbb{M}(\chi,\zeta)$$
 (B3)

Appendix C: Expression of the Strain Energy Release Rate

In the following, we seek to express explicitly the thermodynamic force $\mathcal{G}_{\rho}^{c,r}$ that is work-conjugated to the crack density ρ^r (for crack inclusions in direction r). From Equation 27, we have:

$$\mathcal{G}_{\rho}^{r} = -\frac{\partial \Psi(E, \rho^{r})}{\partial \rho^{r}} = -\frac{1}{2}E : \frac{\partial \mathbb{C}^{\text{hom}}}{\partial \rho^{r}} : E + \sum_{i \in B, D} f_{i} \boldsymbol{\pi}_{i} : \frac{\partial \mathbb{A}_{i}^{r}}{\partial \rho^{r}} : E \\
-\frac{1}{2} \sum_{i,j \in B, D} f_{i} \boldsymbol{\pi}_{i} : \frac{\partial \mathbb{D}_{ij}}{\partial \rho^{r}} : \mathbb{C}_{j}^{-1} : \boldsymbol{\pi}_{j}$$
(C1)

In the following, we calculate $\partial_{\rho}^{r}\mathbb{C}^{\text{hom}}$, $\partial \rho^{r}\mathbb{A}'_{i}$ and $\partial \rho^{r}\mathbb{D}_{ij}$.

From Equations 17 and 19, the homogenized stiffness tensor can be written as:

$$\mathbb{C}^{\text{hom}} = \langle \mathbb{C} : \mathbb{A} \rangle$$

$$= f_D \mathbb{C}_D : \mathbb{A}'_D + \sum_{k=1}^{N_b} f_b^k \mathbb{C}_b^k : \mathbb{A}_b^{k,'}$$
(C2)

We thus have:

$$\frac{\partial \mathbb{C}^{\text{hom}}}{\partial \rho^r} = f_D \left(\frac{\partial \mathbb{C}_D}{\partial \rho^r} : \mathbb{A}_D' + \mathbb{C}_D : \frac{\partial \mathbb{A}_D'}{\partial \rho^r} \right) + \\
+ \sum_{k=1}^{N_b} f_b^k \mathbb{C}_b^k : \frac{\partial \mathbb{A}_b^{k,\prime}}{\partial \rho^r} \tag{C3}$$

From Equation 26, it is readily seen that (Dormieux & Kondo, 2009; Dormieux et al., 2006):

$$\mathbb{S}^{D} = \left(f_{m} \mathbb{I} + \sum_{r \in \mathcal{O}} \frac{4\pi \rho^{r}}{3} \mathbb{T}^{r} + \sum_{r \in \mathcal{CL}} \frac{4\pi \rho^{r}}{3} \mathbb{T}^{\prime,r} \right) : \mathbb{S}_{m}$$
 (C4)

in which \mathbb{S}_m and \mathbb{S}_D are the matrix compliance tensor (i.e., the inverse of \mathbb{C}_m), and the damaged compliance tensor (i.e., the inverse of \mathbb{C}_D), respectively. We thus have:

$$\forall r \in \mathcal{C}, \quad \frac{\partial \mathbb{S}_D}{\partial \rho^r} = \frac{4\pi}{3} \mathbb{T}^r : \mathbb{S}_m \tag{C5}$$

From Equation B3 in Appendix B, we find that:

$$\frac{\partial \mathbb{C}_D}{\partial \rho^r} = -\mathbb{C}_D : \mathbb{H}^r : \mathbb{C}_D \tag{C6}$$

XU ET AL. 31 of 37

with

$$\mathbb{H}^r = \frac{4\pi}{3} \mathbb{T}^r : \mathbb{S}_m \tag{C7}$$

From Equation 11, we have:

$$\mathbb{A}_i' = \mathbb{A}_i^{o,i'} : \left(\sum_{j \in B, D} f_j \mathbb{A}_j^{o,i'}\right)^{-1} \tag{C8}$$

in which:

$$\mathbb{A}_{D}^{o,\prime} = \mathbb{I} \tag{C9}$$

$$\mathbb{A}_{b}^{o,k,'} = \left[\mathbb{I} + \mathbb{P}_{b}^{k,i} : \left(\mathbb{C}_{b}^{k,'} - \mathbb{C}_{D} \right) \right]^{-1} \tag{C10}$$

$$\sum_{j \in B, D} f_j \mathbb{A}_j^{o,'} = f_D \mathbb{I} + \sum_{k=1}^{N_b} f_b^k \mathbb{A}_b^{o, k,'}$$
 (C11)

From Equation B3 in Appendix B, we have:

$$\frac{\partial \mathbb{A}_{b}^{o,k,'}}{\partial \rho^{r}} = -\mathbb{A}_{b}^{o,k,'} : \frac{\partial \left[\mathbb{I} + \mathbb{P}_{b}^{k,i} : \left(\mathbb{C}_{b}^{k,'} - \mathbb{C}_{D} \right) \right]}{\partial \rho^{r}} : \mathbb{A}_{b}^{o,k,'}$$

$$= \mathbb{A}_{b}^{o,k,'} : \left(-\frac{\partial \mathbb{P}_{b}^{k,i}}{\partial \rho^{r}} : \mathbb{C}_{b}^{k,'} + \frac{\partial \mathbb{P}_{b}^{k,i}}{\partial \rho^{r}} : \mathbb{C}_{D} + \mathbb{P}_{b}^{k,i} : \frac{\partial \mathbb{C}_{D}}{\partial \rho^{r}} \right) : \mathbb{A}_{b}^{o,k,'}$$
(C12)

in which $\partial_{\rho^r} \mathbb{P}_b^{k,i}$ is calculated numerically using Finite Difference Method.

Additionally, we have:

$$\frac{\partial \sum_{j \in B, D} f_j \mathbb{A}_j^{s,'}}{\partial \rho^r} = \sum_{k=1}^{N_b} f_b^k \frac{\partial \mathbb{A}_b^{o, k,'}}{\partial \rho^r}$$
(C13)

and therefore:

$$\frac{\partial \left(\sum_{j \in B,D} f_{j} \mathbb{A}_{j}^{o,'}\right)^{-1}}{\partial \rho^{r}} = -\left(\sum_{j \in B,D} f_{j} \mathbb{A}_{j}^{o,'}\right)^{-1} : \frac{\partial \sum_{j \in B,D} f_{j} \mathbb{A}_{j}^{o,'}}{\partial \rho^{r}}
: \left(\sum_{j \in B,D} f_{j} \mathbb{A}_{j}^{o,'}\right)^{-1}$$
(C14)

In Equation C3, we have:

$$\frac{\partial \mathbb{A}'_{D}}{\partial \rho^{r}} = \frac{\partial \left(\sum_{j \in B, D} f_{j} \mathbb{A}_{j}^{o,'}\right)^{-1}}{\partial \rho^{r}}$$
(C15)

and

$$\frac{\partial \mathbb{A}_{b}^{k,'}}{\partial \rho^{r}} = \frac{\partial \mathbb{A}_{b}^{o,k,'}}{\partial \rho^{r}} : \left(\sum_{j \in B,D} f_{j} \mathbb{A}_{j}^{o,'} \right)^{-1} + \\
\mathbb{A}_{b}^{o,k,'} : \frac{\partial \left(\sum_{j \in B,D} f_{j} \mathbb{A}_{j}^{o,'} \right)^{-1}}{\partial \rho^{r}} \tag{C16}$$

XU ET AL. 32 of 37



Note that in Equation C1, the term $\sum_{i \in B,D} f_i \pi_i : \partial_{\rho^r} \mathbb{A}'_i : E$ only needs to be calculated for the phases with eigenstrain, that is, for the biotite-like inclusions (because for phases without eigenstrain, $\pi_i = \mathbf{0}$). Hence, that term can be calculated from the expression of $\partial_{\rho^r} \mathbb{A}^{k,'}_{b}$ in Equation C16.

The last term to calculate is $\partial_{\rho^r} \mathbb{D}_{ij}$. In Equation C1, the term $-\frac{1}{2} \sum_{i,j \in \mathcal{B}, D} f_i \pi_i : \partial_{\rho^r} \mathbb{D}_{ij} : \mathbb{C}_j^{-1} : \pi_j$ also only needs to be calculated for the inclusions with eigenstrain. Let us calculate $\partial_{\rho^r} \mathbb{D}_{ij}$ in that term. For the *i*th and *j*th phases with eigenstrains $(I, J \in \mathcal{B})$:

$$\mathbb{D}_{ij} = \left\{ \underbrace{\left[\delta_{ij} \mathbb{I} - f_{j} \mathbb{A}'_{i} \right] : \mathbb{A}_{j}^{o,'} : \mathbb{P}'_{j}}_{A} + \underbrace{\left[\mathbb{A}'_{i} : < \mathbb{A}^{o,'} : \mathbb{P}' > - \mathbb{A}_{i}^{o,'} : \mathbb{P}'_{j} \right] : < (\mathbb{C}^{\text{hom}} - \mathbb{C}) : \mathbb{A}^{o,'} : \mathbb{P}' >^{-1} :}_{C} \right.$$

$$f_{j} : \underbrace{\left[\left(\mathbb{I} - \mathbb{A}'_{j} \right)^{T} + \left(\mathbb{C}^{\text{hom}} - \mathbb{C}_{j} \right) : \mathbb{A}_{j}^{o,'} : \mathbb{P}'_{j} \right]}_{D} \right\} : \mathbb{C}_{j}$$
(C17)

We have:

$$\frac{\partial \mathbb{D}_{ij}}{\partial \rho^r} = \left\{ \frac{\partial A}{\partial \rho^r} + \frac{\partial B}{\partial \rho^r} : C : f_j D + B : \frac{\partial C}{\partial \rho^r} : f_j D + B : C : f_j \frac{\partial D}{\partial \rho^r} \right\} : \mathbb{C}_j$$
 (C18)

Since crack inclusions are not endowed with any eigenstrain, many partial derivatives cancel out, and we have:

$$\frac{\partial A}{\partial \rho'} = \delta_{ij} \mathbb{I} : \left(\frac{\partial A_{j}^{\alpha'}}{\partial \rho'} : \mathbb{P}'_{j} + A_{j}^{\alpha'} : \frac{\mathbb{P}'_{j}}{\partial \rho'} \right) - f_{J} \left(\frac{\partial A_{j}^{\alpha'}}{\partial \rho'} : A_{j}^{\alpha'} : \mathbb{P}'_{j} \right) \\
+ A'_{i} : \frac{\partial A_{j}^{\alpha'}}{\partial \rho'} : \mathbb{P}'_{j} + A'_{i} : A_{j}^{\alpha'} : \frac{\partial \mathbb{P}'_{j}}{\partial \rho r} \right) \\
\frac{\partial B}{\partial \rho'} = \frac{\partial A_{i}^{\gamma}}{\partial \rho'} : < A^{\alpha'} : \mathbb{P}' > + A'_{i} : \frac{\partial < A^{\alpha'} : \mathbb{P}' >}{\partial \rho'} \\
- \left(\frac{\partial A_{j}^{\alpha'}}{\partial \rho'} : \mathbb{P}'_{i} + A_{i}^{\alpha'} : \frac{\partial \mathbb{P}'_{j}}{\partial \rho'} \right) \\
- \left(\frac{\partial A_{j}^{\alpha'}}{\partial \rho'} : \mathbb{P}'_{i} + A_{i}^{\alpha'} : \frac{\partial \mathbb{P}'_{j}}{\partial \rho'} \right) \\
= \left(\frac{\partial C^{-1}}{\partial \rho'} - \frac{\partial C_{j}}{\partial \rho'} \right) : A_{j}^{\alpha'} : \mathbb{P}'_{j} + \left(\mathbb{C}^{\text{hom}} - \mathbb{C}_{b} \right) : \frac{\partial A_{j}^{\alpha'}}{\partial \rho'} : \mathbb{P}'_{b} + \left(\mathbb{C}^{\text{hom}} - \mathbb{C}_{b} \right) : A_{j}^{\alpha'} : \mathbb{P}'_{b} \right] \\
= \left(\frac{\partial C^{\text{hom}}}{\partial \rho'} - \frac{\partial C_{D}}{\partial \rho'} \right) : A_{j}^{\alpha'} : \mathbb{P}'_{j} + \left(\mathbb{C}^{\text{hom}} - \mathbb{C}_{b} \right) : \frac{\partial A_{j}^{\alpha'}}{\partial \rho'} : \mathbb{P}'_{b} + \left(\mathbb{C}^{\text{hom}} - \mathbb{C}_{b} \right) : A_{j}^{\alpha'} : \mathbb{P}'_{b} \right) \\
+ \sum_{k=1}^{N_{b}} f_{k}^{b} \left\{ \left(\frac{\partial C^{\text{hom}}}{\partial \rho'} - \frac{\partial C_{b}^{b}}{\partial \rho'} \right) : A_{j}^{\alpha'} : \mathbb{P}'_{b} + \left(\mathbb{C}^{\text{hom}} - \mathbb{C}_{b}^{k} \right) : \frac{\partial A_{j}^{\alpha'}}{\partial \rho'} : \mathbb{P}'_{b} \right) \\
+ \left(\mathbb{C}^{\text{hom}} - \mathbb{C}_{b}^{b} \right) : A_{j}^{\alpha'} : \frac{\partial \mathbb{P}'_{b}}{\partial \rho'} \right\} \\
\frac{\partial C}{\partial \rho'} = -C : \frac{\partial C^{-1}}{\partial \rho'} : C \\
\frac{\partial D}{\partial \rho'} = -\left(\frac{\partial A_{j}^{a}}{\partial \rho'} \right)^{T} + \frac{\partial}{\partial \rho'} \left[\left(\mathbb{C}^{\text{hom}} - \mathbb{C}_{j} \right) : A_{j}^{\alpha'} : \mathbb{P}'_{j} \right] \\
= -\left(\frac{\partial A_{j}^{a}}{\partial \rho'} \right)^{T} + \left(\frac{\partial C^{\text{hom}}}{\partial \rho'} - \frac{\partial C_{j}}{\partial \rho'} \right) : A_{j}^{\alpha'} : \mathbb{P}'_{j} \right) \\
+ \left(\mathbb{C}^{\text{hom}} - \mathbb{C}_{j} \right) : \frac{\partial A_{j}^{\alpha'}}{\partial \rho'} : \mathbb{P}'_{j} + \left(\mathbb{C}^{\text{hom}} - \mathbb{C}_{j} \right) : A_{j}^{\alpha'} : \frac{\partial \mathbb{P}'_{j}}{\partial \rho'} \right)$$

in which $\partial_{\rho^r}\mathbb{C}_D$, $\partial_{\rho^r}\mathbb{C}^{\text{hom}}$, $\partial_{\rho^r}\mathbb{A}_i^{o,'}$ and $\partial_{\rho^r}\mathbb{A}_i'$ can be calculated from Equations C3, C6, C12, C15, and C16. At this point, the combination of Equations C1, C3, C15, C16, C18, and C19 provides the explicit expression of $\mathcal{G}_{\rho}^{c,r}$.

XU ET AL. 33 of 37



Appendix D: Calculation of the Tangent Stiffness Tensor for Finite Element Simulations

The differentiation of the stress strain relationship can be derived from Equation 16. Considering that the changes of biotite stiffness due to weathering $\Delta \mathbb{C}_b$ are small in front of the variations of the eigenstrains $\Delta \eta_b$, and recognizing that all the partial derivatives of \mathbb{C}^{hom} can be expressed as composed derivatives of the crack densities ρ^r , we have:

$$\Delta \Sigma = \mathbb{C}^{\text{hom}} : \Delta E + \Delta \mathbb{C}^{\text{hom}} : E - \sum_{k=1}^{N_b} f_b^k \mathbb{C}_b^k : \left(\boldsymbol{\eta}_b^k : \Delta \mathbb{A}_b^{k,'} + \Delta \boldsymbol{\eta}_b^k : \mathbb{A}_b^{k,'} \right) \\
= \mathbb{C}^{\text{hom}} : \Delta E + \sum_{r \in J_{\text{act}}} \frac{\partial \mathbb{C}^{\text{hom}}}{\partial \rho^r} \Delta \rho^r : E \\
- \sum_{k=1}^{N_b} f_b^k \mathbb{C}_b^k : \left(\boldsymbol{\eta}_b^k : \sum_{r \in J_{\text{act}}} \frac{\partial \mathbb{A}_b^{k,'}}{\partial \rho^r} \Delta \rho^r + \Delta \boldsymbol{\eta}_b^k : \mathbb{A}_b^{k,'} \right)$$
(D1)

The crack density increment for each crack set is obtained from the discrete consistency condition on the damage criterion given in Equation 28:

$$\forall r \in \mathcal{J}_{act}, \quad \partial_{\Sigma} g^r : \Delta \Sigma + \partial_{\rho^r} g^r \cdot \Delta \rho^r = 0$$
 (D2)

By substituting Equation D2 into Equation D1, the tangent stiffness tensor $\mathbb{C}^{tg} = \partial \Delta \Sigma / \partial \Delta E$ can be obtained as:

$$\mathbb{C}^{Ig} = \frac{\partial \Delta \Sigma}{\partial \Delta E} \\
= \mathbb{C}^{\text{hom}} + \sum_{r \in \mathcal{J}_{\text{act}}} \frac{\partial \mathbb{C}^{\text{hom}}}{\partial \rho^r} : \left(\frac{\partial \Delta \rho^r}{\partial \Delta E} : E \right) \\
- \sum_{k=1}^{N_b} f_b^k \mathbb{C}_b^k \eta_b^k : \left(\sum_{r \in \mathcal{J}_{\text{act}}} \frac{\partial \mathbb{A}_b^{k,r}}{\partial \rho^r} : \frac{\partial \Delta \rho^r}{\partial \Delta E} \right)$$
(D3)

in which:

$$\frac{\partial \Delta \rho^{r}}{\partial \Delta E} = \frac{\partial \Delta \rho^{r}}{\partial \Delta \Sigma} : \frac{\partial \Delta \Sigma}{\partial \Delta E}
= -\frac{\partial_{\Sigma} g^{r}}{\partial_{\sigma^{r}} g^{r}} : \mathbb{C}^{tg}$$
(D4)

Notation

a	crack radius
a_0	initial crack radius
c	crack half opening
c_0	initial crack half opening
$e_i (i = 1, 2, 3)$	vector basis at the REV scale
e'_i ($i = 1, 2, 3$)	vector basis at the biotite scale
f	volume fraction of phase
g	damage criterion
<u>n</u>	normal vector to crack plane
$v_{ m m}$	molar volume of weathered biotite
N	number of phases in the REV
$N_{ m b}$	number of biotite inclusion phases in the REV
$N_{\rm c}$	number of crack inclusion phases in the REV
K	lateral stress coefficient
Q	number of moles of weathered biotite in the REV
R	chemical weathering rate of biotite per unit mineral surface area
$R_{\rm c}$	maximum resistance parameter
S	total biotite surface area within the REV

XU ET AL. 34 of 37



$V_{ m b}$	remaining unweathered biotite
V_b^w	weathered biotite volume in the inclusion
$V_{ m b,initial}$	initial volume of nonweathered biotite
X	= c/a, aspect ratio of crack
\boldsymbol{E}	macroscopic strain tensor
\boldsymbol{E}_0	far field strain
R	projection tensor
A	strain concentration tensor
\mathbb{A}^o	infinite strain concentration tensor
\mathbb{C}	microscopic elastic stiffness tensor
\mathbb{C}^{tg}	tangent stiffness tensor
$\mathbb{C}^{\mathrm{hom}}$	homogenized elastic stiffness tensor
\mathbb{C}^D	homogenized stiffness tensor of the crack-matrix system
\mathbb{C}^o_c	elastic stiffness tensor of open cracks
\mathbb{C}^{cl}_c	elastic stiffness tensor of closed cracks
D	influence tensor
0	fourth-order unit tensor
J	fourth-order hydrostatic projection tensor
K	fourth-order deviatoric projection tensor
P	Hill polarization tensor
ρ	crack density variable
$ ho_{ m c}$	critical crack density parameter
$ ho^0$	initial crack density parameter
γ	rock specific density
ψ , θ , ϕ	Euler angles
δ	Kronecker delta
ϵ	microscopic strain tensor
$\boldsymbol{\epsilon}^m$	average strain field of the matrix phase
η	local eigenstrain tensor
π	local eigenstress tensor
σ	microscopic stress tensor
$oldsymbol{\Sigma}$	macroscopic stress tensor
Ψ	strain energy of the REV
Ω	second-order damage tensor
${f \Omega}^0$	initial damage value
) damage components along \underline{x}_1 , \underline{x}_2 and \underline{x}_3 directions
$\mathcal{G}_{ ho}$	damage driving force
\mathcal{N}	number of cracks per unit volume
$\mathcal R$	material's resistance to damage

Data Availability Statement

The material point simulations in Section 4 are conducted using MATLAB. Regarding the Finite Element model, we use ABAQUS with UMAT subroutine. The MATLAB code and Fortran code are available at https://github.gatech.edu/txu90/CodeforJGR.

Acknowledgments

This work was supported by the U.S. National Science Foundation under grant EAR-1755321 ("Collaborative research: Microscopic fracturing and macroscopic weakening: A novel model for bedrock fracturing by biotite weathering") to Ferrier, Arson, and West.

References

Anderson, R. S., Anderson, S. P., & Tucker, G. E. (2013). Rock damage and regolith transport by frost: An example of climate modulation of the geomorphology of the critical zone. *Earth Surface Processes and Landforms*, 38(3), 299–316. https://doi.org/10.1002/esp.3330

Arson, C. (2020). Micro-macro mechanics of damage and healing in rocks. *Open Geomechanics*, 2, 1–41. https://doi.org/10.5802/ogeo.4

Bažant, P., & Oh, B. (1986). Efficient numerical integration on the surface of a sphere. *ZAMM-Journal of Applied Mathematics and Mechanics/ Zeitschrift für Angewandte Mathematik und Mechanik*, 66(1), 37–49. https://doi.org/10.1002/zamm.19860660108

Behrens, R., Bouchez, J., Schuessler, J. A., Dultz, S., Hewawasam, T., & von Blanckenburg, F. (2015). Mineralogical transformations set slow weathering rates in low-porosity metamorphic bedrock on mountain slopes in a tropical climate. *Chemical Geology*, 411, 283–298. https://doi.org/10.1016/j.chemgeo.2015.07.008

XU ET AL. 35 of 37



- Benveniste, Y. (1987). A new approach to the application of Mori-Tanaka's theory in composite materials. *Mechanics of Materials*, 6(2), 147–157. https://doi.org/10.1016/0167-6636(87)90005-6
- Benveniste, Y., Dvorak, G., & Chen, T. (1991). On diagonal and elastic symmetry of the approximate effective stiffness tensor of heterogeneous media. *Journal of the Mechanics and Physics of Solids*, 39(7), 927–946. https://doi.org/10.1016/0022-5096(91)90012-d
- Bouchez, J. L. (1997). Granite is never isotropic: An introduction to AMS studies of granitic rocks. In *Granite: From segregation of melt to emplacement fabrics* (pp. 95–112). Springer.
- Brantut, N., Baud, P., Heap, M., & Meredith, P. (2012). Micromechanics of brittle creep in rocks. *Journal of Geophysical Research: Solid Earth*, 117(B8), B08412. https://doi.org/10.1029/2012jb009299
- Brantut, N., Heap, M., Meredith, P., & Baud, P. (2013). Time-dependent cracking and brittle creep in crustal rocks: A review. *Journal of Structural Geology*, 52, 17–43. https://doi.org/10.1016/j.jsg.2013.03.007
- Bunge, H.-J. (2013). Texture analysis in materials science: Mathematical methods, Elsevier.
- Buss, H. L., Brantley, S. L., Scatena, F., Bazilievskaya, E., Blum, A., Schulz, M., et al. (2013). Probing the deep critical zone beneath the Luquillo Experimental Forest, Puerto Rico. Earth Surface Processes and Landforms, 38(10), 1170–1186. https://doi.org/10.1002/esp.3409
- Buss, H. L., Sak, P. B., Webb, S. M., & Brantley, S. L. (2008). Weathering of the Rio Blanco quartz diorite, Luquillo Mountains, Puerto Rico: Coupling oxidation, dissolution, and fracturing. Geochimica et Cosmochimica Acta, 72(18), 4488–4507. https://doi.org/10.1016/j. gca.2008.06.020
- Callahan, R. P., Ferrier, K. L., Dixon, J., Dosseto, A., Hahm, W. J., Jessup, B. S., et al. (2019). Arrested development: Erosional equilibrium in the southern Sierra Nevada, California, maintained by feedbacks between channel incision and hillslope sediment production. *GSA Bulletin*, 131(7–8), 1179–1202. https://doi.org/10.1130/b35006.1
- Callahan, R. P., Riebe, C. S., Pasquet, S., Ferrier, K. L., Grana, D., Sklar, L. S., et al. (2020). Subsurface weathering revealed in hillslope-integrated porosity distributions. *Geophysical Research Letters*, 47(15), e2020GL088322. https://doi.org/10.1029/2020gl088322
- Chen, T., Dvorak, G. J., & Benveniste, Y. (1992). Mori-Tanaka estimates of the overall elastic moduli of certain composite materials. *Journal of Applied Mechanics*, 59(3), 539–546. https://doi.org/10.1115/1.2893757
- Dai, L., Huang, Z., & Wang, R. (1998). A generalized self-consistent Mori-Tanaka scheme for prediction of the effective elastic moduli of hybrid multiphase particulate composites. *Polymer Composites*, 19(5), 506–513. https://doi.org/10.1002/pc.10125
- Desrumaux, F., Meraghni, F., & Benzeggagh, M. (2001). Generalised Mori-Tanaka scheme to model anisotropic damage using numerical Eshelby tensor. *Journal of Composite Materials*, 35(7), 603–624. https://doi.org/10.1177/002199801772662091
- Deudé, V., Dormieux, L., Kondo, D., & Pensée, V. (2002). Propriétés élastiques non linéaires d'un milieu mésofissuré. Comptes Rendus Mecanique, 330(8), 587–592. https://doi.org/10.1016/s1631-0721(02)01489-4
- Dixon, J. L., Hartshorn, A. S., Heimsath, A. M., DiBiase, R. A., & Whipple, K. X. (2012). Chemical weathering response to tectonic forcing: A soils perspective from the San Gabriel Mountains, California. *Earth and Planetary Science Letters*, 323, 40–49. https://doi.org/10.1016/j.epsl.2012.01.010
- Dixon, J. L., Heimsath, A. M., & Amundson, R. (2009). The critical role of climate and saprolite weathering in landscape evolution. *Earth Surface Processes and Landforms*, 34(11), 1507–1521. https://doi.org/10.1002/esp.1836
- Dong, H., Peacor, D. R., & Murphy, S. F. (1998). Tem study of progressive alteration of igneous biotite to kaolinite throughout a weathered soil profile. *Geochimica et Cosmochimica Acta*, 62(11), 1881–1887. https://doi.org/10.1016/s0016-7037(98)00096-9
- Dormieux, L., & Kondo, D. (2009). Stress-based estimates and bounds of effective elastic properties: The case of cracked media with unilateral effects. *Computational Materials Science*, 46(1), 173–179. https://doi.org/10.1016/j.commatsci.2009.02.027
- Dormieux, L., Kondo, D., & Ulm, F.-J. (2006). Microporomechanics. John Wiley & Sons.
- Eppes, M.-C., & Keanini, R. (2017). Mechanical weathering and rock erosion by climate-dependent subcritical cracking. *Reviews of Geophysics*, 55(2), 470–508. https://doi.org/10.1002/2017rg000557
- Eppinger, B., Hayes, J. L., Carr, B., Moon, S., Cosans, C., Holbrook, W., et al. (2021). Quantifying depth-dependent seismic anisotropy in the critical zone enhanced by weathering of a piedmont schist. *Journal of Geophysical Research: Earth Surface*, 126(10), e2021JF006289. https://doi.org/10.1029/2021jf006289
- Eshelby, J. D. (1957). The determination of the elastic field of an ellipsoidal inclusion, and related problems. *Proceedings of the Royal Society of London A*, 241(1226), 376–396.
- Ferrier, K. L., Riebe, C. S., & Jesse Hahm, W. (2016). Testing for supply-limited and kinetic-limited chemical erosion in field measurements of regolith production and chemical depletion. Geochemistry, Geophysics, Geosystems, 17(6), 2270–2285. https://doi.org/10.1002/2016gc006273
- Fletcher, R., Buss, H. L., & Brantley, S. L. (2006). A spheroidal weathering model coupling porewater chemistry to soil thicknesses during steady-state denudation. *Earth and Planetary Science Letters*, 244(1–2), 444–457. https://doi.org/10.1016/j.epsl.2006.01.055
- Flinchum, B. A., Steven Holbrook, W., Rempe, D., Moon, S., Riebe, C. S., Carr, B. J., et al. (2018). Critical zone structure under a granite ridge inferred from drilling and three-dimensional seismic refraction data. *Journal of Geophysical Research: Earth Surface*, 123(6), 1317–1343. https://doi.org/10.1029/2017jf004280
- Gavazzi, A., & Lagoudas, D. (1990). On the numerical evaluation of Eshelby's tensor and its application to elastoplastic fibrous composites. Computational Mechanics, 7(1), 13–19. https://doi.org/10.1007/bf00370053
- Goodfellow, B. W., Hilley, G. E., Webb, S. M., Sklar, L. S., Moon, S., & Olson, C. A. (2016). The chemical, mechanical, and hydrological evolution of weathering granitoid. *Journal of Geophysical Research: Earth Surface*, 121(8), 1410–1435. https://doi.org/10.1002/2016jf003822
 Graham, R., Tice, K., & Guertal, W. R. (1994). The pedologic nature of weathered rock. *Whole Regolith Pedology*, 34, 21–40.
- Hayes, J. L., Riebe, C. S., Holbrook, W. S., Flinchum, B. A., & Hartsough, P. C. (2019). Porosity production in weathered rock: Where volumetric strain dominates over chemical mass loss. *Science Advances*, 5(9), eaao0834. https://doi.org/10.1126/sciadv.aao0834
- Heimsath, A. M., & Whipple, K. X. (2019). Strength matters: Resisting erosion across upland landscapes. Earth Surface Processes and Landforms, 44(9), 1748–1754. https://doi.org/10.1002/esp.4609
- Hewawasam, T., von Blanckenburg, F., Bouchez, J., Dixon, J. L., Schuessler, J. A., & Maekeler, R. (2013). Slow advance of the weathering front during deep, supply-limited saprolite formation in the tropical highlands of Sri Lanka. *Geochimica et Cosmochimica Acta*, 118, 202–230.
- https://doi.org/10.1016/j.gca.2013.05.006

 Holbrook, W. S., Marcon, V., Bacon, A. R., Brantley, S. L., Carr, B. J., Flinchum, B. A., et al. (2019). Links between physical and chemical weathering inferred from a 65-m-deep borehole through earth's critical zone. Scientific Reports. 9(1), 1–11. https://doi.org/10.1038/s41598-019-40819-9
- Isherwood, D., & Street, A. (1976). Biotite-induced grussification of the Boulder Creek Granodiorite, Boulder County, Colorado. *The Geological Society of America Bulletin*, 87(3), 366–370. https://doi.org/10.1130/0016-7606(1976)87<366:bgotbc>2.0.co;2
- Jiang, H., & Lee, C.-T. A. (2019). On the role of chemical weathering of continental arcs in long-term climate regulation: A case study of the Peninsular Ranges batholith, California (USA). Earth and Planetary Science Letters, 525, 115733. https://doi.org/10.1016/j.epsl.2019.115733

XU ET AL. 36 of 37



- Kachanov, M. (1992). Effective elastic properties of cracked solids: Critical review of some basic concepts. Applied Mechanics Reviews, 45(8), 304–335. https://doi.org/10.1115/1.3119761
- Laws, N. (1973). On the thermostatics of composite materials. Journal of the Mechanics and Physics of Solids, 21(1), 9–17. https://doi.org/10.1016/0022-5096(73)90027-6
- Leone, J. D., Holbrook, W. S., Riebe, C. S., Chorover, J., Ferré, T. P., Carr, B. J., & Callahan, R. P. (2020). Strong slope-aspect control of regolith thickness by bedrock foliation. Earth Surface Processes and Landforms, 45(12), 2998–3010. https://doi.org/10.1002/esp.4947
- Meraghni, F., Desrumaux, F., & Benzeggagh, M. (2002). Implementation of a constitutive micromechanical model for damage analysis in glass mat reinforced composite structures. Composites Science and Technology, 62(16), 2087–2097. https://doi.org/10.1016/s0266-3538(02)00110-0
- Miller, D. J., & Dunne, T. (1996). Topographic perturbations of regional stresses and consequent bedrock fracturing. *Journal of Geophysical Research*, 101(B11), 25523–25536. https://doi.org/10.1029/96jb02531
- Molnar, P. (2004). Interactions among topographically induced elastic stress, static fatigue, and valley incision. *Journal of Geophysical Research*, 109(F2), F02010. https://doi.org/10.1029/2003jf000097
- Moon, S., Perron, J., Martel, S., Holbrook, W., & St. Clair, J. (2017). A model of three-dimensional topographic stresses with implications for bedrock fractures, surface processes, and landscape evolution. *Journal of Geophysical Research: Earth Surface*, 122(4), 823–846. https://doi. org/10.1002/2016jf004155
- Moon, S., Perron, J. T., Martel, S. J., Goodfellow, B. W., Mas Ivars, D., Hall, A., et al. (2020). Present-day stress field influences bedrock fracture openness deep into the subsurface. *Geophysical Research Letters*, 47(23), e2020GL090581. https://doi.org/10.1029/2020gl090581
- Mori, T., & Tanaka, K. (1973). Average stress in matrix and average elastic energy of materials with misfitting inclusions. *Acta Metallurgica*, 21(5), 571–574. https://doi.org/10.1016/0001-6160(73)90064-3
- Mura, T. (1987). Micromechanics of defects in solids. Martinus Niihoff.
- Nasseri, M., Mohanty, B., & Robin, P.-Y. (2005). Characterization of microstructures and fracture toughness in five granitic rocks. *International Journal of Rock Mechanics and Mining Sciences*, 42(3), 450–460. https://doi.org/10.1016/j.ijrmms.2004.11.007
- Nasseri, M., Schubnel, A., & Young, R. (2007). Coupled evolutions of fracture toughness and elastic wave velocities at high crack density in thermally treated Westerly granite. *International Journal of Rock Mechanics and Mining Sciences*, 44(4), 601–616. https://doi.org/10.1016/j. iirmms.2006.09.008
- Nettleton, W., Flach, K., & Nelson, R. (1970). Pedogenic weathering of tonalite in southern California. Geoderma, 4(4), 387–402. https://doi.org/10.1016/0016-7061(70)90055-8
- Novitsky, C. G., Holbrook, W. S., Carr, B. J., Pasquet, S., Okaya, D., & Flinchum, B. A. (2018). Mapping inherited fractures in the critical zone using seismic anisotropy from circular surveys. Geophysical Research Letters, 45(7), 3126–3135. https://doi.org/10.1002/2017gl075976
- Pavich, M. J., Leo, G., Obermeier, S., & Estabrook, J. R. (1989). Investigations of the characteristics, origin, and residence time of the upland residual mantle of the piedmont of Fairfax County, Virginia. (Tech. Rep.).
- Pichler, B., & Hellmich, C. (2010). Estimation of influence tensors for eigenstressed multiphase elastic media with nonaligned inclusion phases of arbitrary ellipsoidal shape. *Journal of Engineering Mechanics*, 136(8), 1043–1053. https://doi.org/10.1061/(asce)em.1943-7889.0000138
- Riebe, C. S., Callahan, R. P., Granke, S. B.-M., Carr, B. J., Hayes, J. L., Schell, M. S., & Sklar, L. S. (2021). Anisovolumetric weathering in granitic saprolite controlled by climate and erosion rate. *Geology*, 49(5), 551–555. https://doi.org/10.1130/g48191.1
- Roering, J. J. (2008). How well can hillslope evolution models "explain" topography? Simulating soil transport and production with high-resolution topographic data. *The Geological Society of America Bulletin*, 120(9–10), 1248–1262. https://doi.org/10.1130/b26283.1
- Roering, J. J., Marshall, J., Booth, A. M., Mort, M., & Jin, Q. (2010). Evidence for biotic controls on topography and soil production. Earth and Planetary Science Letters, 298(1–2), 183–190. https://doi.org/10.1016/j.epsl.2010.07.040
- Salve, R., Rempe, D. M., & Dietrich, W. E. (2012). Rain, rock moisture dynamics, and the rapid response of perched groundwater in weathered, fractured argillite underlying a steep hillslope. Water Resources Research, 48(11), 11528. https://doi.org/10.1029/2012wr012583
- Schoenball, M., Sahara, D. P., & Kohl, T. (2014). Time-dependent brittle creep as a mechanism for time-delayed wellbore failure. *International Journal of Rock Mechanics and Mining Sciences*, 70, 400–406. https://doi.org/10.1016/j.ijrmms.2014.05.012
- Shen, X., Arson, C., Ferrier, K. L., West, N., & Dai, S. (2019). Mineral weathering and bedrock weakening: Modeling microscale bedrock damage under biotite weathering. *Journal of Geophysical Research: Earth Surface*, 124(11), 2623–2646. https://doi.org/10.1029/2019jf005068
- Slim, M., Perron, J. T., Martel, S. J., & Singha, K. (2015). Topographic stress and rock fracture: A two-dimensional numerical model for arbitrary topography and preliminary comparison with borehole observations. Earth Surface Processes and Landforms, 40(4), 512–529. https://doi.org/10.1002/esp.3646
- St. Clair, J., Moon, S., Holbrook, W., Perron, J., Riebe, C., Martel, S., et al. (2015). Geophysical imaging reveals topographic stress control of bedrock weathering. *Science*, 350(6260), 534–538. https://doi.org/10.1126/science.aab2210
- Stefanou, I., & Sulem, J. (2014). Chemically induced compaction bands: Triggering conditions and band thickness. *Journal of Geophysical Research: Solid Earth*, 119(2), 880–899. https://doi.org/10.1002/2013jb010342
- Stock, G. M., Martel, S. J., Collins, B. D., & Harp, E. L. (2012). Progressive failure of sheeted rock slopes: The 2009–2010 Rhombus Wall rock falls in Yosemite Valley, California, USA. Earth Surface Processes and Landforms, 37(5), 546–561. https://doi.org/10.1002/esp.3192
- Vierra, E., Webb, H., & Girty, G. (2018). Unravelling the development of a spheroidally weathered diorite-gabbro, Santa Margarita Ecological
- Reserve, Peninsular Ranges, southern California, USA. Catena, 163, 297–310. https://doi.org/10.1016/j.catena.2017.12.033
 Wahrhaftig, C. (1965). Stepped topography of the southern Sierra Nevada, California. The Geological Society of America Bulletin, 76(10),
- Walder, J., & Hallet, B. (1985). A theoretical model of the fracture of rock during freezing. *The Geological Society of America Bulletin*, 96(3), 336–346. https://doi.org/10.1130/0016-7606(1985)96<336:atmotf>2.0.co;2
- Walker, J. C., Hays, P., & Kasting, J. F. (1981). A negative feedback mechanism for the long-term stabilization of Earth's surface temperature. Journal of Geophysical Research, 86(C10), 9776–9782. https://doi.org/10.1029/jc086ic10p09776
- Watakabe, T., & Matsushi, Y. (2019). Lithological controls on hydrological processes that trigger shallow landslides: Observations from granite and hornfels hillslopes in Hiroshima, Japan. Catena, 180, 55–68. https://doi.org/10.1016/j.catena.2019.04.010
- White, A. F., & Brantley, S. L. (2003). The effect of time on the weathering of silicate minerals: Why do weathering rates differ in the laboratory and field. Chemical Geology, 202(3-4), 479-506. https://doi.org/10.1016/j.chemgeo.2003.03.001

XU ET AL. 37 of 37

1165-1190. https://doi.org/10.1130/0016-7606(1965)76[1165:stotss]2.0.co;2